Steady streaming: A key mixing mechanism in low-Reynolds-number acinar flows

Haribalan Kumar,[1] Merryn H. Tawhai,[2] Eric A. Hoffman,[3] and Ching-Long Lin[1,a)]
[1]*Department of Mechanical and Industrial Engineering, The University of Iowa, Iowa City, Iowa 52242, USA and IIHR-Hydroscience and Engineering, The University of Iowa, Iowa City, Iowa 52242, USA*
[2]*Bioengineering Institute, The University of Auckland, Auckland 1010, New Zealand*
[3]*Department of Biomedical Engineering, The University of Iowa, Iowa City, Iowa 52242, USA; Department of Internal Medicine, The University of Iowa, Iowa City, Iowa 52242, USA; and Department of Radiology, The University of Iowa, Iowa City, Iowa 52242, USA*

(Received 27 June 2010; accepted 14 February 2011; published online 18 April 2011)

Study of mixing is important in understanding transport of submicron sized particles in the acinar region of the lung. In this article, we investigate transport in view of advective mixing utilizing Lagrangian particle tracking techniques: tracer advection, stretch rate and dispersion analysis. The phenomenon of steady streaming in an oscillatory flow is found to hold the key to the origin of kinematic mixing in the alveolus, the alveolar mouth and the alveolated duct. This mechanism provides the common route to folding of material lines and surfaces in any region of the acinar flow, and has no bearing on whether the geometry is expanding or if flow separates within the cavity or not. All analyses consistently indicate a significant decrease in mixing with decreasing Reynolds number (Re). For a given Re, dispersion is found to increase with degree of alveolation, indicating that geometry effects are important. These effects of Re and geometry can also be explained by the streaming mechanism. Based on flow conditions and resultant convective mixing measures, we conclude that significant convective mixing in the duct and within an alveolus could originate only in the first few generations of the acinar tree as a result of nonzero inertia, flow asymmetry, and large Keulegan–Carpenter (K_C) number. © *2011 American Institute of Physics*. [doi:10.1063/1.3567066]

I. INTRODUCTION

Several studies have attempted to identify mechanisms of mixing in low-Re flows. Some of the earlier works in this regard are Refs. 1–7 and among others. The application areas include transport of material in processing industries, mixers, microfluidic applications, and physiological flows. In addition to these applications, the study of mixing is important in understanding the transport of particles in the conducting and respiratory regions of the lung. Understanding of transport to and within the acinar region has practical applications in improving delivery strategies of pharmaceutical aerosols or other drugs, targeting deposition to specific locations and henceforth reducing systemic absorption, and also for improving estimates for retention of inhaled pollutants. Without the assistance of turbulent mixing, how the low-Re acinar flow achieves effective mixing is the topic of interest in this paper.

Lung morphology and relevant terminologies are introduced here. Alveoli are air pockets that occupy a part of, or completely cover the walls of respiratory airways; on average beyond the 15th generation of the human airway tree. An "acinus" consists of the entire region of alveoli and alveolated ducts that are distal to the terminal bronchus. The alveoli can be visualized as an isolated or group of open cavities ventilated by the acinar airway. The typical Re ranges approximately from 2 in the transitional region to 0.01 in the terminal sacs. For further reading on acinar morphology and morphometry, the reader is referred to Refs. 8 and 9.

During normal breathing, when the inspired volume is larger than the anatomical deadspace, the inspired gas "mixes" with the residual gas in the lung. In this process, particles are transferred to the residual gas across the inspired-residual interface front, which in case of aerosols is referred to as aerosol mixing. Peclet number ($\mathrm{Pe}=U_0D/K$, where U_0 is the mean fluid velocity, D is the duct diameter, and K is the diffusion coefficient) relates the magnitude of convective to diffusive transport. For gas mixing in the acinus, $\mathrm{Pe}\approx 0.1-1$, while for aerosol particles (say, ~ 1 μm diameter), $\mathrm{Pe}=3000-20\,000$. Consequently, convection and diffusion manifest differently in these two mixing processes.[10]

Particles with diameter $0.5-1$ μm have very low deposition efficiencies in the acinus and behave like nondiffusing massless fluid particles.[11] Particles in this size range play a very important role in various physiological processes.[12] Heyder *et al.* performed mixing estimates with aerosol bolus consisting of ~ 1 μm particles.[13] The dispersion of the inhaled bolus increased with increasing penetration volume. The net transport of particles from the (particle-laden) inspired air to the residual air was shown to occur as a result of irreversible processes whose origins were unknown. This motivated investigations of possible transport mechanisms

a)Author to whom correspondence should be addressed. Present address: Department of Mechanical and Industrial Engineering, The University of Iowa, Iowa City, Iowa 52242-1527, USA. Tel.: +13193355673. FAX: +13193355669. Electronic mail: ching-long-lin@uiowa.edu.

and their origin. The accomplishment of mixing, particularly in viscous flows deep in the lung are nontrivial. Advective mixing was proposed as one such mechanism.

The early proponents of various acinar mixing mechanisms within alveoli include Refs. 14–18. Tsuda *et al.* and Henry *et al.* observed mixing in particle motion associated with recirculation in an acinar model.[14,18] Tsuda *et al.* performed experimental flow visualization in a rat lung using blue and white colored dyes for inspired and resident fluids.[15] Lateral images of acinar airways revealed delineated interface patterns between the two dyes. After four breathing cycles, an indistinguishable blue-white uniformity appeared indicating a high degree of mixing. Recently, Henry *et al.* demonstrated that alveolation is sufficient to produce convective mixing in a rigid-wall oscillatory flow model with Re pertaining to proximal generations of the acinus.[19] This observation completely shifts the onus from mixing originating due to time-dependent wall motion and saddle point as thought earlier. It also shifts the focus toward geometrical features apart from revealing that even fundamental mixing mechanisms are not completely understood. Sarangapani and Wexler commented that the contribution from mixing toward a dramatic increase in the interface area requires numerous cycles and hence cannot completely explain the observed dispersion in a single cycle.[20] Other works include those of Lee and Lee, who used 30 identical toroidal alveolar cells and modeled inspiration and expiration in isolated phases.[21] The differences in dispersion between alveolated and nonalveolated tubes in the presence and absence of wall motion were compared. From previous experimental and numerical studies, although various possible causes have been suggested, consistent and concrete evidence to origins of convective mixing in the acinus is still missing. Darquenne and Prisk compared dispersion of aerosol bolus between simulation and experiments.[22] For particles of critical sizes 0.5 and 1 μm in diameter, order-of-magnitude discrepancy was observed in a zero-gravity environment. Flow-induced mixing was suggested as one possible cause. Later, Darquenne and Prisk designed a flow reversal (FR) mechanism to study the mixing in acinar flow.[23] Boli of particles were inhaled in microgravity at two different penetration volumes. It was then followed by a breathhold during which several flow reversals were imposed. They found that "either the phenomenon of stretch and fold did not occur within the number of FR… or that it had already occurred during the one breathing cycle included in the basic maneuver."

Dispersion and mixing of aerosol boluses may be sufficiently modeled by simple advection. The difference in fluid particle location between the beginning and end of one oscillatory flow cycle may be recognized as a drift in a Lagrangian sense. This drift, large or small, is gained by a particle purely due to flow topology, inertial and geometry effects. Through-out this work, streaming and the associated drift will be underlined as the fundamental mechanism. In acinar flows, the flow conditions cause a large drift and hence large increases in dye interface area from one cycle to the next, which is commonly referred to as advective mixing. Even though pure advection is considered, the term "kinematic irreversibility"[18] is more commonly used in this context, which in essence is the Lagrangian drift at the end of one cycle.

The objective of this work is to investigate the origin of advective mixing and quantify mixing in physiologically motivated models of the acinus using three Lagrangian techniques: tracer advection, stretching analysis, and axial dispersion. Unlike previous acinar mixing studies whose attention was restricted to a specific region, this paper considers mixing in three regions: the duct, the alveolar mouth, and the alveolus. Of the three techniques, tracer advection and stretching analysis provide a measure of the mixing rate within the alveolus. The topological critical points, such as a stagnation saddle point in the flow, are also identified for assessing their roles in mixing from the viewpoint of chaotic mixing.[14,15] The study of acinar mixing is not complete without understanding axial transport in the alveolated duct. Axial dispersion and effective diffusivity are estimated in the alveolated airways. The remainder of the paper is organized as follows. Section II describes the model and equations for the different analysis techniques. Section III presents the results. For clarity, we first use a simple two-dimensional (2D) alveolated channel to illustrate some important, but not well understood, dispersion and mixing mechanisms in a low-Re multiple-open-cavity model before considering a three-dimensional (3D) geometry. Section IV summarizes conclusions and discusses physiological implications.

II. METHODS

A. Lagrangian methods

Geometrical structures that are representative of different regions of the acinus, namely respiratory bronchioles and alveolar ducts are shown in Fig. 1. Henceforth, we use "Case I" [Fig. 1(a)] to denote respiratory bronchioles which have occasional alveoli. "Case II" [Fig. 1(b)] is a model for alveolar duct lined completely with 18 alveoli representing the lung units in generations 18–22. The alveolar duct is well defined in Case I. On the other hand, the walls of the duct in Case II are not clearly defined and are formed from the space between surrounding alveoli. The proximal wall of the alveolus is conventionally the one closest to the alveolus mouth during inspiration. Similarly the proximal generation is the generation of airways, which has already been ventilated along the path of the air. Analogously, a distal wall and a distal generation are defined. To simulate the alveolar flow, a sinusoidal flow rate is specified at the ductal entrance "E" in Figs. 1(a) and 1(b). The walls of alveoli and duct expand and contract uniformly with a prescribed volumetric expansion of 25%. The Reynolds number ($\mathrm{Re}=U_0D/\nu$) is measured at peak inspiration, where U_0 is the average peak inspiratory speed at the ductal entrance, D is the effective diameter of the duct, and ν is the kinematic viscosity of air. The incompressible Navier–Stokes equations are solved in an Arbitrary Lagrangian–Eulerian framework.[24,25] The equations are normalized using the alveolus mouth dimension of $L=416$ μm and peak velocity of $U_0=0.032$ m/s. A sinusoidal flow rate is specified at one end of the duct while a Neumann boundary condition is employed at the other. Homothetic wall motion, where corresponding sides of the duct and al-

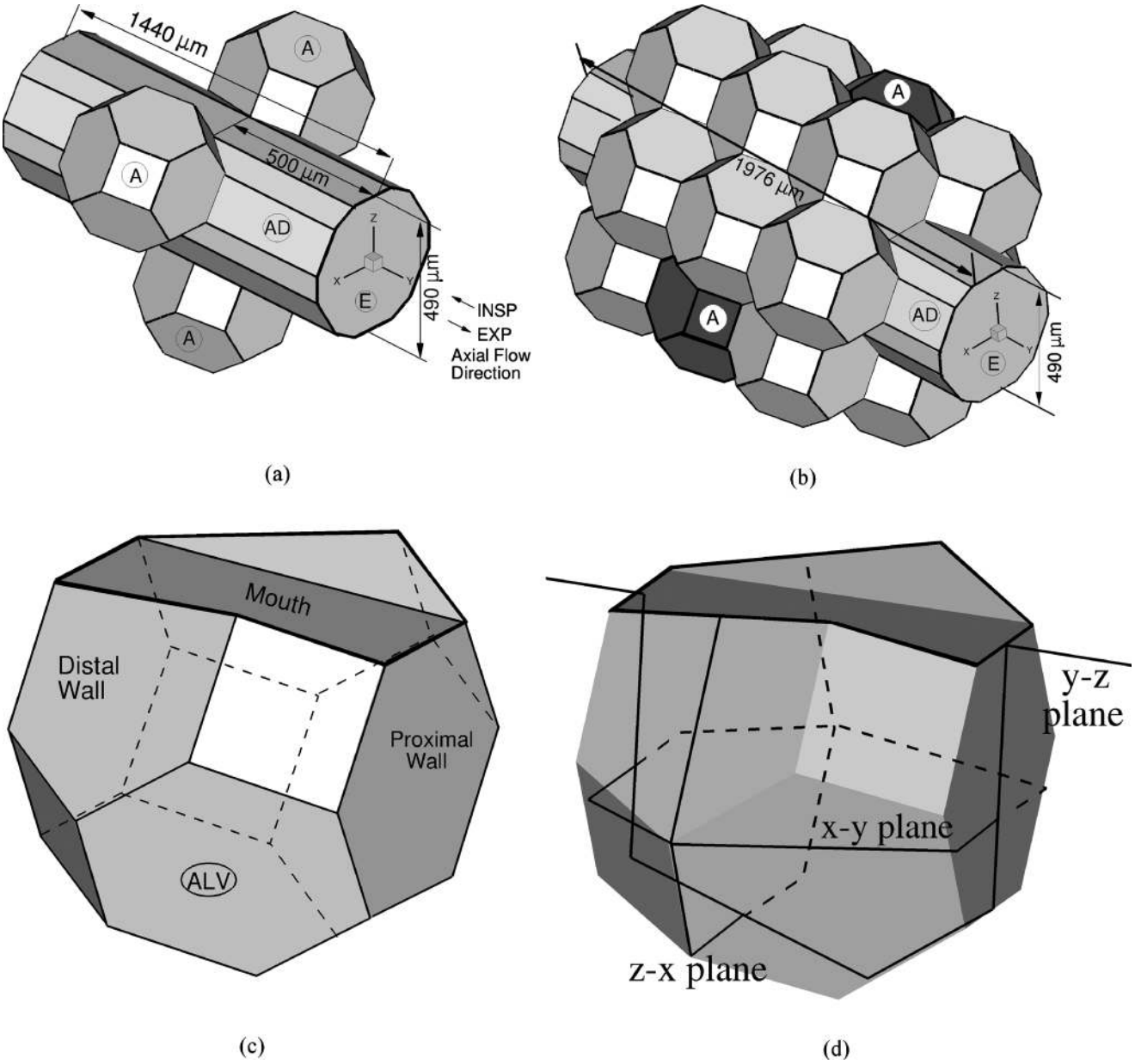

FIG. 1. Representative geometrical models for regions of the acinus. (a) "Case I" model for respiratory bronchiole, (b) "Case II" model for alveolar duct, where (A, AD, and E) denote (alveoli, alveolar duct, and ductal entrance), (c) and (d) shows two presentations of an alveolar sac, denoted by ALV in (a) to be analyzed in Sec. III. (c) ALV with solid and dashed edges for front and rear faces, respectively. (d) ALV with three planes to show the orientation of the unit. The y-direction is the axial direction. Some results are displayed in the *y-z* plane for clarity.

veolar wall remain parallel in a geometric expansion or contraction is prescribed. The domain is discretized using tetrahedral elements with a smallest element having a size of $\sim 0.009L$. A single alveolar unit consists of ~40 000 elements. For a detailed description of the computational method and boundary conditions, the reader is referred to Kumar *et al.*[26] The breathing period (T) is chosen as 2.5 s (at 24 breaths/min) to match the Womersley number ($W_o = D\sqrt{\omega/\nu} = 0.2$, $\omega = 2\pi/T$ is the angular frequency) in previous studies.[14,19] The inverse of Strouhal number (St) is known as Keulegan–Carpenter number,[27] $K_C = 1/St = U_0 T/L$. It determines the displacement or length of fluid particle excursion over a characteristic length, L. For analysis, Case I (with Re=2, 1, and 0.52) and Case II (with Re=1, 0.6, and 0.2) are investigated. For Case I, Re=2, 1, and 0.52 yield K_C of 386, 193, and 96.5, respectively. An additional case with Re=0.06 of Case I is included to demonstrate that advection with Re approaching zero, predicted by the current analysis, exhibits essentially reversible behaviors. The flow phenomena along the acinar pathway are commonly associated with the fractional flow rate Q_A/Q_D introduced by Tsuda *et al.*[14] Here, Q_A is the alveolar flow rate and Q_D is the ductal entrance flow rate. Note that in a rigid-wall model, $Q_A/Q_D = 0$. The amount of alveolar expansion determines Q_A while the volume change rate of the air volume in generations distal to the current generation determines Q_D. This ratio, by definition increases down the acinar tree. For example, based on the ductal flow rate in Case I, $Q_A/Q_D = 0.0024$ for Re=2 and

$Q_A/Q_D=0.0047$ for Re=1. For isolated alveolar representations, we use Q_A/Q_D and Re to identify flow conditions in Cases I and II. For Case I with Re=1, due to nonzero Q_A the Re at the exit of the model is approximately reduced by 4%.

The transport model of small (less than ~ 1 μm) aerosol particles across the interface of residual and inhaled air reduces to advection equation as sedimentational and depositional effects become negligible. Advection is governed by the 3D kinematic vector equation:

$$\frac{d\boldsymbol{x}}{dt}=\boldsymbol{u}(\boldsymbol{x},t),\boldsymbol{x}(0)=\boldsymbol{x}_0, \tag{1}$$

where $\boldsymbol{x}$ is the position vector of a passive particle (sometimes referred as a marker); $\boldsymbol{u}$ is the numerically generated velocity field and $\boldsymbol{x}_0$ is an initial condition. The advection is passive involving no diffusion of particles and the particle velocity exactly matches the fluid velocity. The advection is carried out using a fourth-order Runge–Kutta scheme and a time-step independent solution is ensured with a choice of $\Delta t=T/500\,000$. For details on a typical procedure to solve for particle transport, the reader is referred to Wang *et al.*[28] All simulations are carried up to five cycles unless specified otherwise.

The mixing measures used in this study are designed to clarify the role of flow topology and geometry in the process of tracer transport. Three independent techniques have been used: tracer advection, stretching analysis, and axial dispersion. Each of these is chosen toward a specific objective and has relative advantages. All three techniques are based on massless particle tracking. The formulation details are given below. Material advection (i.e., tracer deformation) involves passive tracking of tracers placed at strategic locations in a flow. The tracer or dye is constructed from a uniform distribution of particles. The second technique, stretch rate analysis, is based on evolution of unit line elements computed from velocity and its gradient. This technique is an extension of the line element approach in Roberts and Mackley (1995)[29] to 3D. Note that particle advection could also be used to compute stretch rate by considering relative separation distance of adjacent particles, which however is a lower-order approximation as it relies on only fluid velocity and fails in high stretch regions.[29] The stretch rate computation based on the line element approach relies on higher-order approximation using fluid velocity and its gradient. In this approach, each particle location is tagged with line elements, following:[29]

$$\frac{D\mathbf{m}}{Dt}=\mathbf{m}\,.\,\nabla\mathbf{u}\text{-}(\underline{D}:\mathbf{mm})\mathbf{m},$$

$$\frac{D(\ln\lambda)}{Dt}=\underline{D}:\mathbf{mm},$$

$$s_1(nT)=\frac{1}{nT}\int_0^{nT}\left(\frac{D\ln\lambda}{Dt}\right)dt, \tag{2}$$

where $\mathbf{m}=(dx,dy,dz)^{\mathrm{T}}$ is the orientation vector of any line element with $|\mathbf{mm}|=1$; $\mathbf{u}$ is the fluid velocity, $\underline{D}$ is the symmetric stretching tensor, and $D(\ln\lambda)/Dt$ is the stretching function. Time-averaged stretch rate, s_l, is obtained from the instantaneous stretching function (of dimension s^{-1}) averaged from three initially orthogonal line elements.

The third measure of mixing employed here is axial dispersion. In this approach, the variance of particle displacement is calculated based on axial location of particles.[30] The initial condition is a bolus of particles released at the entrance of the alveolar duct. For a bolus consisting of N markers, the axial mean $\langle y\rangle$ and variance σ_y^2 at the end of the nth breathing cycle are defined as

$$\langle y\rangle=\sum_N[y_i(nT)-y_i(t_0)]/N,$$

$$\sigma_y^2=\sum_N\{[y_i(nT)-y_i(t_0)]-\langle y\rangle\}^2/(N-1), \tag{3}$$

where nT is the total time after "n" breathing periods and t_0 may be the initial release time or some reference state, say the end of first breathing period. Because the current acinar model consists of alveoli attached to a straight duct, they represent a section of the acinar tree. A periodic boundary condition is employed so that particles exiting the domain are allowed to reenter thus approximating multiple alveolar units attached to the duct.

B. Eulerian streaming, Stokes drift, and Lagrangian drift velocities

The mechanism of Lagrangian drift outlined here derives its background from the well-known "steady streaming" in oscillatory flows.[27,31–37] In an oscillatory flow setting, a nonzero mean flow averaged over one time period may be observed. This nonzero mean flow can result in significant drift of particles at end cycle called steady streaming. An entire treatise on steady streaming was given by Riley.[33] Suh and Kang presented different instances of streaming and the importance of Stokes drift.[37] Larrieu *et al.* presented an analytical treatment of drift in a simple setting of Couette flow weakly perturbed by a wavy bottom.[34] For any given passive particle under the assumption of small displacement,[37] Eq. (1) with $\boldsymbol{x}(t=0)=\boldsymbol{x}_0$ may be expanded in a Taylor series.

$$\frac{d\boldsymbol{x}}{dt}=\boldsymbol{u}(\boldsymbol{x},t)\approx\boldsymbol{u}(\boldsymbol{x}_0,t)+(\delta\boldsymbol{x}\cdot\nabla)\boldsymbol{u}(\boldsymbol{x}_0,t)+\text{H.O.T.}, \tag{4}$$

where the small displacement $\delta\boldsymbol{x}=\int_0^t\boldsymbol{u}(\boldsymbol{x}_0,t)dt$ and "H.O.T." indicates higher-order terms of the series. Let the time average of a variable ϕ over one period of T be denoted as $\langle\phi\rangle$. Then, to the first-order approximation,

$$\frac{\boldsymbol{x}(T)-\boldsymbol{x}(0)}{T}=\boldsymbol{u}_L(\boldsymbol{x}_0)=\boldsymbol{u}_E(\boldsymbol{x}_0)+\boldsymbol{u}_S(\boldsymbol{x}_0), \tag{5}$$

where $\boldsymbol{u}_E(\boldsymbol{x}_0)=\langle\boldsymbol{u}(\boldsymbol{x}_0,t)\rangle$ and $\boldsymbol{u}_S(\boldsymbol{x}_0)=\langle\delta\boldsymbol{x}\cdot\nabla\boldsymbol{u}(\boldsymbol{x}_0,t)\rangle$. $\boldsymbol{u}_E$ is known as the "Eulerian mean" (or "Eulerian streaming") velocity and $\boldsymbol{u}_S$ is the "Stokes drift" velocity. $\boldsymbol{u}_L$, which is the sum of $\boldsymbol{u}_E$ and $\boldsymbol{u}_S$, is called the "Lagrangian mean" (or "Lagrangian streaming" or "Lagrangian drift") velocity. Lagrangian streaming is often referred to as steady streaming. Conceptually the decomposition of $\boldsymbol{u}(\boldsymbol{x},t)=\boldsymbol{u}(\boldsymbol{x}_0,t)+(\delta\boldsymbol{x}\cdot\nabla)\boldsymbol{u}(\boldsymbol{x}_0,t)$ or $\boldsymbol{u}_L=\boldsymbol{u}_E+\boldsymbol{u}_S$ resembles the material deriva-

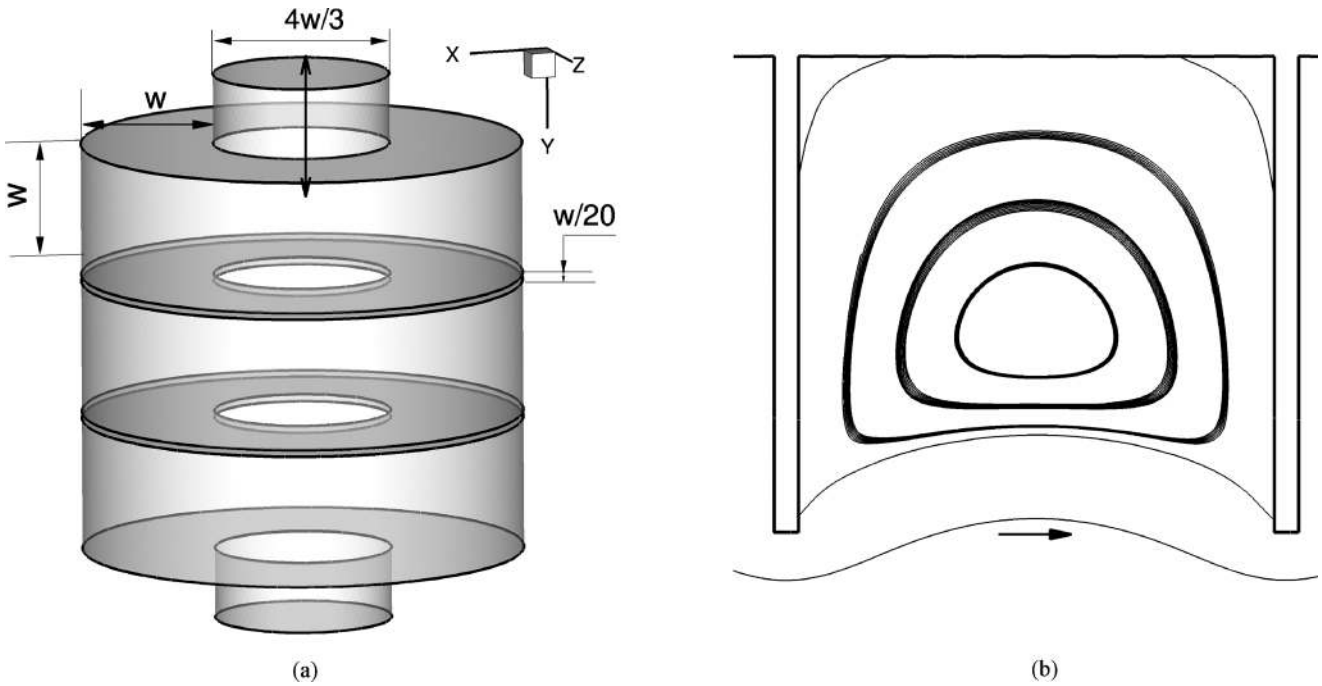

FIG. 2. (a) An axisymmetric alveolated duct model used for validation. The model geometry and dimensions are chosen from Henry *et al.* (Ref. 19). (b) Streamlines in the cross-section of an axisymmetric alveolus near peak inspiration.

tive $D\phi/Dt=\partial\phi/\partial t+\boldsymbol{u}\cdot\nabla\phi$ in a Lagrangian framework that consists of a local derivative (the former) and a convective derivative (the latter). More precisely, the acceleration of a fluid parcel is obtained by taking the time derivative of Eq. (4), which yields the material derivative of the parcel's velocity. Although steady streaming is a nonlinear phenomenon, the Eulerian streaming is caused by the fluid dynamical interaction (between fluid parcels and with the geometry of the fluid system under consideration) and the Stokes drift arises from a kinematic viewpoint, depending on the pathline of the tracked particle.[37] The decomposition Eq. (5) allows distinction between the two effects. Nonetheless, Eq. (5) holds true only when the displacement of a particle is small such that $\boldsymbol{u}(\boldsymbol{x},t)$ can be expanded in series with respect to the initial reference location $\boldsymbol{x}_o$. Typically, acinar flows are characterized by a large K_C number. Hence the above differential form of Eq. (5) must be modified in discrete form for large particle displacements. Consider a particle at a location $\boldsymbol{x}_j$ at $t_j=j\Delta t$ with $\Delta t=T/N$. To the first-order approximation of the Taylor series expansion of Eq. (1), the generalized stencil for the particle location is as follows:

$$\frac{\boldsymbol{x}_1-\boldsymbol{x}_0}{\Delta t}=\boldsymbol{u}(\boldsymbol{x}_0,t_0)\quad\text{for}\quad P=1, \tag{6}$$

$$\frac{\boldsymbol{x}_P-\boldsymbol{x}_{P-1}}{\Delta t}=\boldsymbol{u}(\boldsymbol{x}_0,t_{P-1})+\boldsymbol{u}_I\quad\text{for}\quad P=2,N,$$

where the "instantaneous" Stokes drift velocity at time t_{P-1} reads

$$\boldsymbol{u}_I=[(\boldsymbol{x}_1-\boldsymbol{x}_0)\cdot\nabla]\boldsymbol{u}(\boldsymbol{x}_0,t_{P-1})+[(\boldsymbol{x}_2-\boldsymbol{x}_1)\cdot\nabla]\boldsymbol{u}(\boldsymbol{x}_1,t_{P-1})+\cdots+[(\boldsymbol{x}_{P-1}-\boldsymbol{x}_{P-2})\cdot\nabla]\boldsymbol{u}(\boldsymbol{x}_{P-2},t_{P-1}).$$

Summation of the above discrete equations for $P=1$ to N gives

$$\frac{\boldsymbol{x}_N-\boldsymbol{x}_0}{T}=\frac{1}{N}\sum_{i=1}^{N}\boldsymbol{u}(\boldsymbol{x}_0,t_{i-1})+\sum_{j=1}^{N}\left\{[(\boldsymbol{x}_j-\boldsymbol{x}_{j-1})\cdot\nabla]\times\left[\frac{1}{N}\sum_{i=j+1}^{N}\boldsymbol{u}(\boldsymbol{x}_{j-1},t_{i-1})\right]\right\}, \tag{7}$$

where $\boldsymbol{u}_L=(\boldsymbol{x}_N-\boldsymbol{x}_0)/T$ is the Lagrangian streaming velocity, $\boldsymbol{u}_E=(1/N)\Sigma_{i=1}^{N}\boldsymbol{u}(\boldsymbol{x}_0,t_{i-1})$ is the Eulerian streaming velocity, and $\boldsymbol{u}_S=\Sigma_{j=1}^{N}\{[(\boldsymbol{x}_j-\boldsymbol{x}_{j-1})\cdot\nabla][(1/N)\Sigma_{i=j+1}^{N}\boldsymbol{u}(\boldsymbol{x}_{j-1},t_{i-1})]\}$ is the Stokes drift velocity.

Furthermore $\boldsymbol{u}_S=\Sigma\boldsymbol{u}_I/N$. For validation of formula (7), please refer to Appendix A.

C. Code validation

Henry *et al.* recently investigated mixing in a stationary wall axisymmetric model to study the effect of unsteadiness induced by the oscillatory flow and nonzero inertia.[19] The flow conditions pertained to proximal generations in the acinus. Their model has been chosen here for validation. The problem details and some of the results are given below. The geometry is a central channel surrounded by three cavities as shown in Fig. 2(a). The solution is obtained for Re=2 ($Q_A/Q_D=0$) and a time period of 3 s. The flow streamlines in the central cavity extracted onto the *y*-*z* plane are shown in

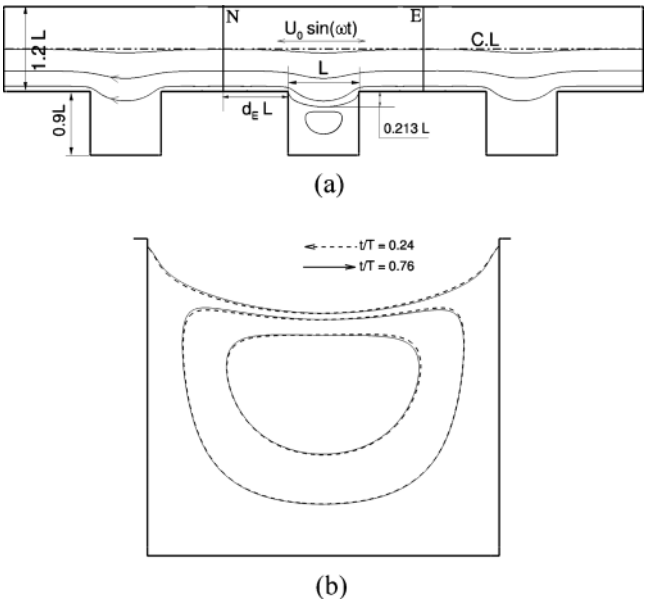

FIG. 3. (a) Schematic of a 2D channel with multiple rectangular cavities. The flow streamlines shown correspond to $t/T=0.24$, close to peak inspiration. d_E is the entrance length parameter. E, model entrance where a parabolic velocity profile is imposed; N, model exit where a Neumann outflow boundary condition is imposed. (b) Streamlines at near peak inspiration ($t/T=0.24$) and expiration ($t/T=0.76$) in the cavity of a channel flow with Re=1. Arrows indicate the axial flow direction in the channel.

Fig. 2(b). Typical of open cavity flows, a single recirculatory flow region is observed in the cavity. A pair of fluid-particles initially separated by an infinitesimal distance of $d_0 \sim 10^{-11}$ are advected for 50 cycles. The rate of separation of this particle pair is estimated by finding the Liapunov exponent given as: $\sigma_n=(1/t)\ln(d_t/d_0)$. Here d_t is the final distance after time t. σ_n converges to a positive value of ~ 0.02 in good agreement with Henry *et al.*[19]

III. RESULTS

A. Flow in a 2D channel

Before embarking on the analysis of flow structure and mixing in the 3D alveolar geometry, a representative 2D case is used to demonstrate various important, but not well-understood, mixing patterns, some of which had been reported before.[10,18] We will first discuss the steady streaming phenomenon and its characteristics, and then relate it to the origin of various interface stretching and folding patterns observed in the duct, in the duct mouth, and within the cavity. Consider an oscillating flow in a 2D long, straight channel with multiple rectangular grooves located periodically on the lower part of the channel as shown in Fig. 3(a). All dimensions and flow conditions are chosen to match closely with Case I. Unlike the 3D cases to be discussed later, the channel and cavity walls remain rigid. Flow is simulated only in the midsection of length $(L+2d_EL)$. Due to low-Re, the flow becomes fully developed within distances much less than one channel height. Hence a parabolic profile with a sinusoidal waveform is imposed at the ductal entrance E, while a Neumann outflow condition is applied at "N." The Re in a 2D setting is defined using the channel height (H) as $\mathrm{Re}=U_0H/\nu$. The simulation is carried out for Re=1 and $K_C=193$. This combination of low-Re and high-K_C is unique for acinar flows. For the given flow conditions, the flow separates and forms one single recirculation eddy in the cavity. The flow structure is not symmetric with respect to the vertical centerline in the cavity as shown in Fig. 3(b) and the deviation from symmetry is resulted from nonzero-Re inertia effects. The flow in the channel is separated from flow in the cavity by a separation line, which attaches itself to the sidewalls of the cavity. This separation line or "separatrix"[7] penetrates roughly to 25% of the cavity depth.

In the following presentation, the advection and observed drift are understood in relation to the Eulerian mean

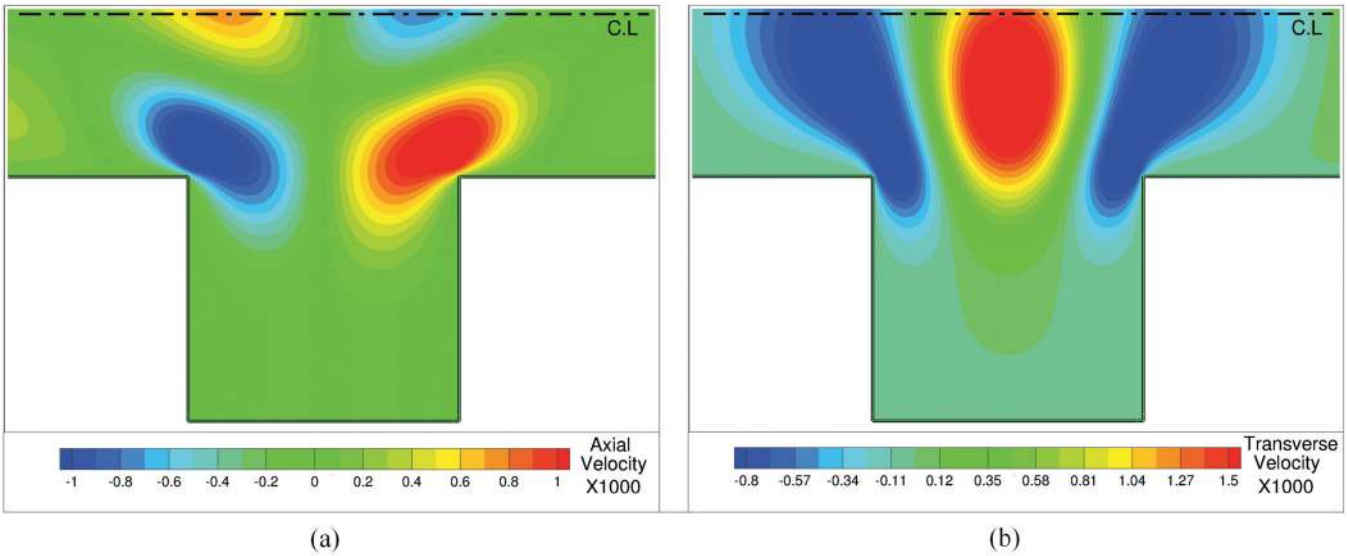

FIG. 4. (Color) Contours of Eulerian mean velocities computed using Eq. (7): (a) axial velocity (y-component) and (b) transverse velocity (x-component).

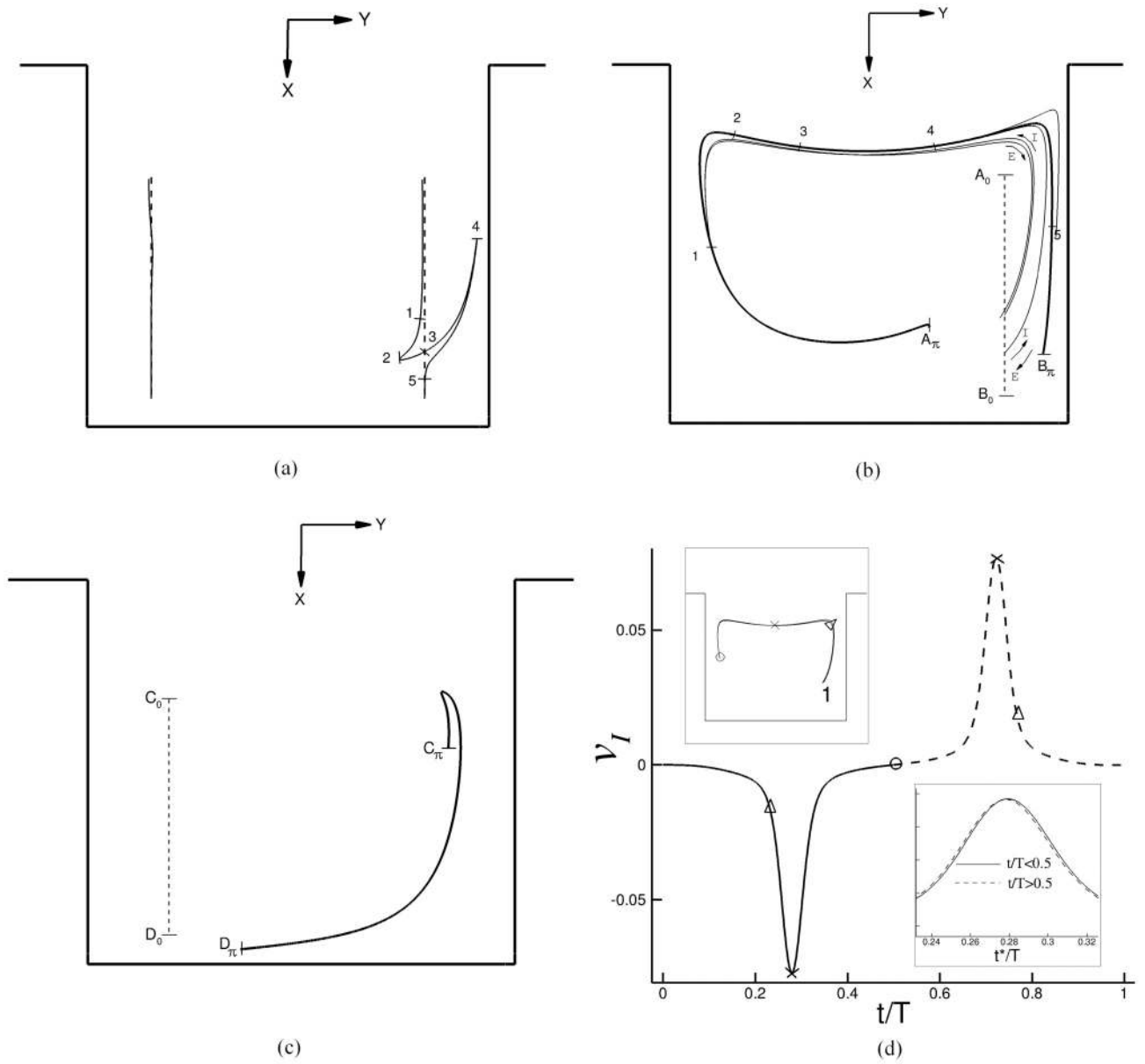

FIG. 5. (a) Drifts (solid line) of two initially vertical line dyes (dotted line) at end cycle $t/T=1$. (b) Location of line dye A_o-B_o at end inspiration $t/T=0.5$, A_π-1-2-3-4-5-B_π. Points 1-2-3-4-5 correspond to those in (a). The pathlines for points 1 and 5 on inspiration and expiration (marked by I and E, respectively) are also plotted. (c) Location of line dye C_o-D_o at end inspiration $t/T=0.5$, C_π-D_π. (d) The distribution of y-component instantaneous Stokes drift velocity v_I for point 1 over one period. The instants at the three locations along the pathlines in the upper left insert are marked by the same symbols in the main plot. In the lower right insert, the inspiratory curve with an inverted sign (solid line) and the expiratory curve with the reversed time $t^*/T=1-t/T$ (dashed line) are overlapped to compare their magnitudes.

TABLE I. Lagrangian streaming, Eulerian mean and Stokes drift velocities for points 1, 2, 3, 4, and 5 inside the cavity marked in Fig. 5(a).

Point	Lagrangian streaming (u_L, v_L)	Eulerian mean (u_E, v_E)	Stokes drift (u_S, v_S)
1	3.943×10^{-005}, -5.693×10^{-005}	-4.681×10^{-006}, 5.807×10^{-006}	4.412×10^{-005}, -6.215×10^{-005}
2	1.478×10^{-004}, -3.257×10^{-004}	-1.244×10^{-006}, 1.751×10^{-006}	1.491×10^{-004}, -3.266×10^{-004}
3	3.931×10^{-007}, 1.919×10^{-006}	-1.022×10^{-006}, 1.455×10^{-006}	1.286×10^{-006}, 9.840×10^{-007}
4	-1.507×10^{-003}, 6.737×10^{-004}	-7.970×10^{-007}, 1.131×10^{-006}	-1.507×10^{-003}, 6.726×10^{-004}
5	-2.253×10^{-006}, 5.470×10^{-006}	-1.295×10^{-007}, 2.309×10^{-009}	-2.121×10^{-006}, 5.467×10^{-006}

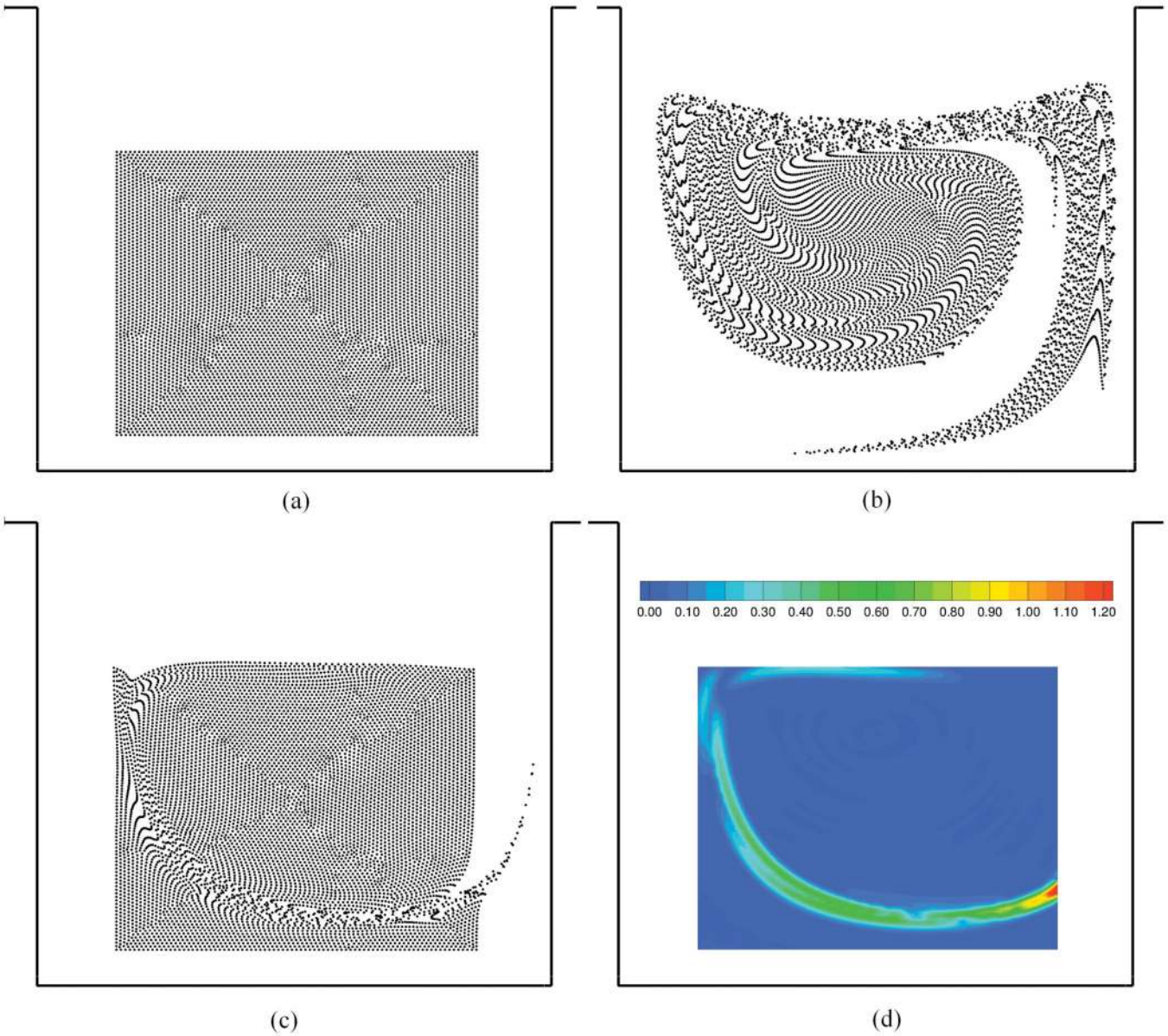

FIG. 6. (Color) Tracer advection in the cavity of a 2D channel flow with Re=1. Distributions of tracer particles at t/T=: (a) 0, (b) 0.5, and (c) 1. (d) Stretch rate map calculated in the same region as (a) within the cavity.

and Stokes drift velocities in Eq. (7). The axial and transverse components of Eulerian mean flow is shown in Fig. 4. Note that the local maximum positive and negative axial Eulerian streaming velocities occur near the two corners of the cavity and are asymmetric in sign with respect to the vertical centerline of the cavity. The nonzero Eulerian streaming components are a result of asymmetries from nonzero-Re inertia effects, which do not cancel out between inspiration and expiration cycles. The distribution of nonzero axial mean in Fig. 4 agrees with the asymmetry of the streamlines shown in Fig. 3(b). Hence, the presence of a nonzero Eulerian mean flow is due to asymmetry in the fluid flow between the two half-cycles and the effect decreases with decreasing Re. On inspiration the fluid flows from right to left, and on expiration the flow is reversed [see Fig. 3(b)]. The flow fields on inspiration and expiration become more asymmetric near the upper corners of the cavity than near the bottom because fluid in the channel experiences immediate expansion and contraction when flowing over the cavity. The Eulerian mean magnitude is about three orders smaller than the mean velocity of the fluid. Such nonzero mean flow effects are typically observed in other low-Re settings such as flow over a wavy bottom. For example, Larrieu *et al.* showed the formation of positive and negative peaks of Eulerian mean velocities observed between two crests of the wavy wall.[34] Because the magnitude of the Eulerian mean velocity $\boldsymbol{u}_E$ is small, to assess the sensitivity of $\boldsymbol{u}_E$ on mesh size we present in Appendix B the comparison of the observed maximum Eulerian mean velocities for three different mesh sizes. The results show that a mesh-independent solution is ensured. The "fine mesh" of Table IV is henceforth used.

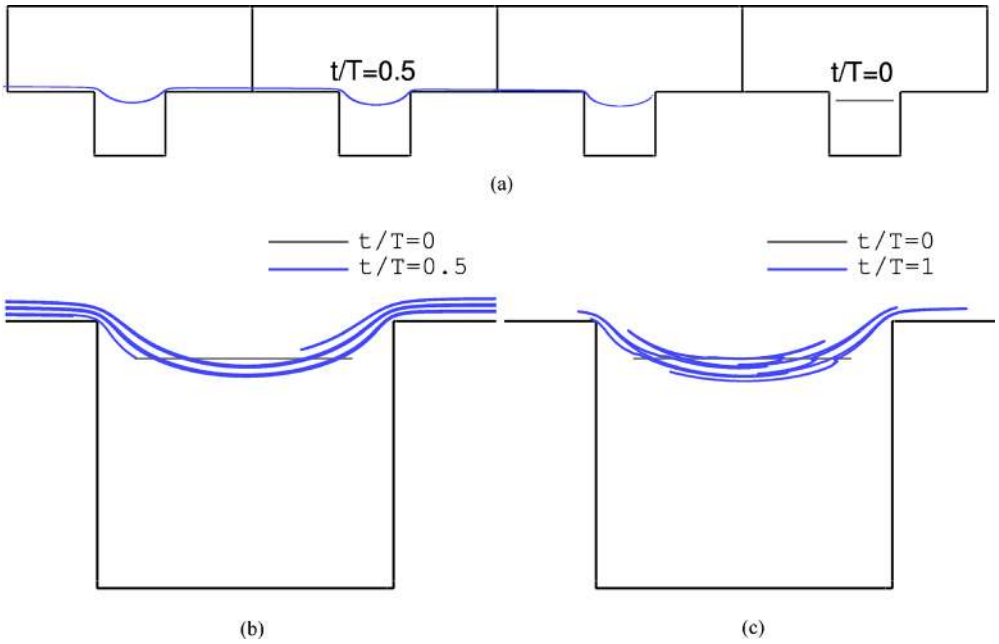

FIG. 7. (Color online) Tracer advection in a 2D channel with d_E=1.2. (a) Advection of an initial line dye (gray) into multiple cavities downstream is shown in blue. (b) Appearance of layer structure at end inspiration t/T=0.5. The dye in multiple cavities shown in (a) is overlaid on to a single cavity due to periodicity. (c) Fold structure is formed after one cycle at t/T=1 and covers the cavity-channel mouth region.

We now consider advection in three regions: the cavity, the cavity-channel mouth, and the outer channel. First, let us consider advection of particles inside the cavity. Let A_0-B_0 and C_0-D_0 denote the respective right and left vertical material lines (comprising a number of Lagrangian particles) at t/T=0 in Fig. 5(a). The drifts of two initial vertical lines of particles at the end of one cycle are also displayed. At end cycle, the right line dye A_0-B_0 forms a fold denoted by 1-2-3-4-5 in Fig. 5(a). On the other hand, the left line dye C_0-D_0 is almost reversed back to its initial location. The shapes of the two dyes at half-cycle t/T=0.5, A_π-B_π and C_π-D_π, are displayed in Figs. 5(b) and 5(c), respectively. The locations of points (Lagrangian particles) 1, 2, 3, 4, and 5 at t/T=1 in Fig. 5(a) are also marked along A_π-B_π at t/T=0.5 in Fig. 5(b). At t/T=0 these points are aligned vertically along A_0-B_0. During inspiration, these points are advected upward toward the mouth region where nonzero streaming is dominant (see Fig. 4). Point 1 is advected to the left wall of the cavity on inspiration, passing through positive and negative streaming zones and resting away from the nonzero streaming zone. The (uppermost) thin line marked by "I" in Fig. 5(b) delineates the pathline of point 1 during forward excursion. On expiration, the pathline E almost follows the inspiratory pathline I, which is expected in very low-Re flow. Points 1 and 5 experience almost zero drift. Points 2, 3, and 4 spread along from negative to positive streaming zones. The resulting Lagrangian drift of the material line at end cycle in Fig. 5(a) takes the shape of a fold with the undershoot of point 2 to the left and the overshoot of point 4 to the right. For the left line C_π-D_π at end inspiration shown in Fig. 5(c), only the tip of the dye reaches the peripheral lower portion of the positive Eulerian streaming zone, producing little drift.

To better understand the roles played by Eulerian mean and Stokes drift on the total (Lagrangian) drift, Table I compares the three terms of Eq. (7): Lagrangian streaming velocity ($\boldsymbol{u}_L$), Eulerian mean velocity ($\boldsymbol{u}_E$), and Stokes drift velocity ($\boldsymbol{u}_S$) for the five points along the right line A_0-B_0. For all the points, the independently calculated $\boldsymbol{u}_L$, $\boldsymbol{u}_E$, and $\boldsymbol{u}_S$ satisfy $\boldsymbol{u}_L \approx \boldsymbol{u}_E + \boldsymbol{u}_S$, (with average error of ~0.15%) again validating Eq. (7). The undershoot of point 2 to the left and the overshoot of point 4 to the right that forms a fold as illustrated in Fig. 5(a) are reflected by the negative and positive y-component steady streaming velocities v_L.

Table I further shows the dominant contribution of Stokes drift to the total drift, suggesting the kinematic (or pathline-dependent) nature of the folding pattern. To further understand this kinematic nature, we shall examine the contribution of the instantaneous Stokes drift velocity $\boldsymbol{u}_I$ in Eq. (6) from various locations along the inspiratory and expiratory pathlines to the total Stokes drift velocity $\boldsymbol{u}_S(=\Sigma \boldsymbol{u}_I/N)$. Figure 5(d) shows the distribution of y-component instantaneous Stokes drift velocity v_I for point 1 (see the insert in the upper left corner where the inspiratory and expiratory pathlines are almost overlapped). On inspiration (solid line) v_I is negative, whereas on expiration (dashed line) v_I becomes positive. The time instants at the three locations along the pathlines in the insert are marked by the same symbols in the main plot. The distributions of v_I on inspiration and expiration are of nearly the same shape, but opposite sign. v_I reaches a local minimum or maximum when the particle reaches around the midway between the left and right walls of the cavity. By inverting the sign of v_I for t/T=0−0.5 and reversing the time axis (t^*/T=1−t/T) for t/T=0.5−1 as shown in the lower right insert, we can compare v_I of the same particle at approximately the same location, but opposite phase. On the left side of the peak value (in the lower

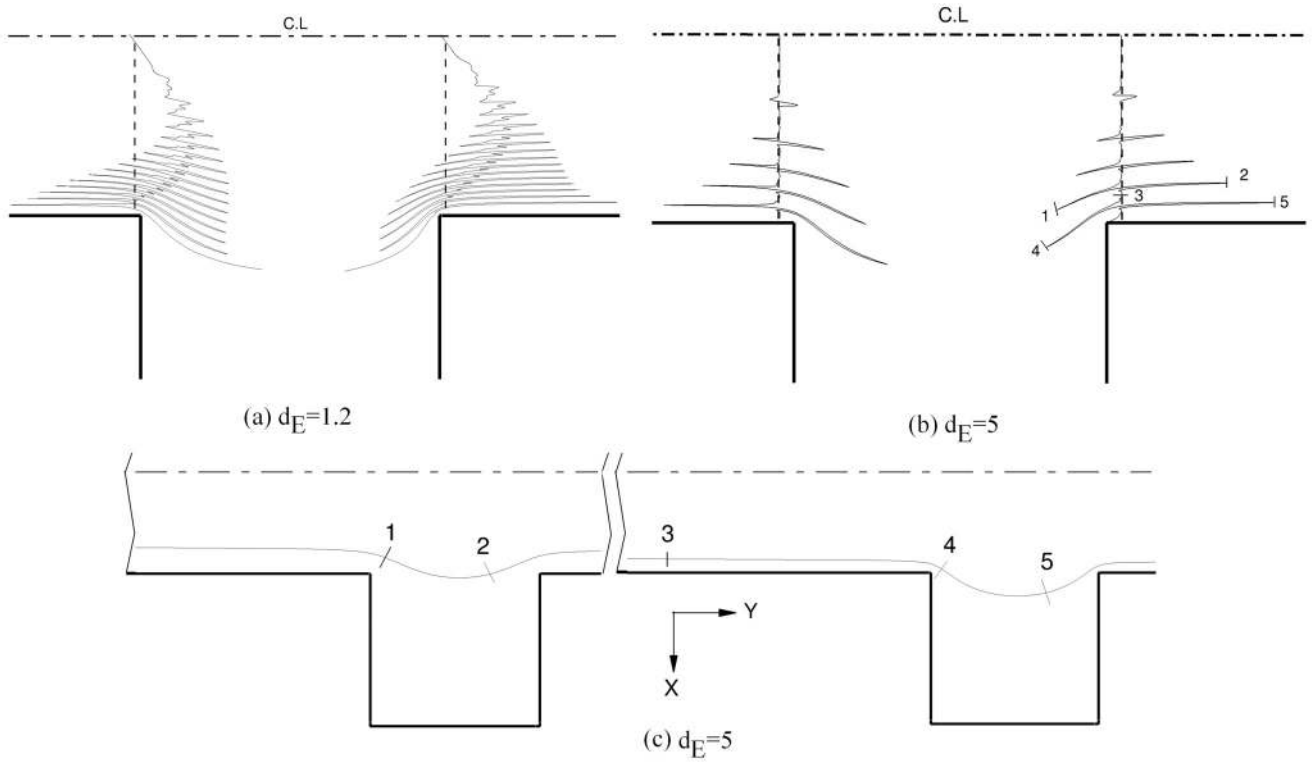

FIG. 8. Drifts of two line dyes in the channel near the two cavity corners for d_E=: (a) 1.2, (b) 5. (c) Locations of points 1-2-3-4-5 at end inspiration t/T =0.5. Their locations at end expiration t/T=1 are marked in (b).

insert), the dashed line is slightly higher than the solid line, signifying the net v_I that contributes to v_S when the particle is near the right upper corner (e.g., the triangle in the upper insert) is positive. On the other hand, on the right side of the peak value, the dashed line is slightly lower than the solid line, resulting in the negative net v_I that the particle experiences near the left upper corner of the cavity. The positive and negative local Stokes drift velocities cancel out at end cycle, resulting in nearly zero displacement in Fig. 5(a) for point 1. This analysis suggests that if a particle is advected through positive and negative Eulerian mean regions and rests at a zero Eulerian mean region at end inspiration t/T =0.5, the total drift at end cycle may be zero due to the cancellation effect.

Next, particle advection and stretch rate maps are demonstrated inside the cavity for two purposes. First, it highlights the connection between particle advection and fluid kinematics reflecting through deformation of line elements expressed by Eq. (2). Second, it helps elucidate the behavior of stretch rate in association with Lagrangian drifts. Figures 6(a)–6(c) show a time sequence of the advection of Lagrangian particles at t/T=0, 0.5, and 1, respectively. Here, the particles initially fill a rectangle, expanding from previous two vertical line dyes to a surface, to map out the drift in the core region of the cavity. At end inspiration [Fig. 6(b)] particles exhibit a spiral shape, equivalent to a combination of Figs. 5(b) and 5(c). At end expiration (i.e., end cycle t/T =1) Fig. 6(c) shows the majority of particles are reversed back to their original locations, except that a series of folds are formed and distributed along a curved strip from the right wall to the bottom wall, and then to the left wall. Figure 6(d) shows the stretch rate map of the same region within the cavity. A tongue of higher stretch rate region surrounds an almost zero mixing core. The higher stretch rate region coincides with the advection map shown in Fig. 6(c), indicating that the stretch rate can capture and distinguish the regions of small and large drifts. A higher stretch rate yields greater separation and fold of dyes.

TABLE II. Lagrangian streaming, Eulerian mean and Stokes drift velocities for points 1, 2, 3, 4, and 5 in the outer channel marked in Fig. 8(b).

Point	Lagrangian streaming (u_L, v_L)	Eulerian mean (u_E, v_E)	Stokes drift (u_S, v_S)
1	3.585×10^{-004}, -1.073×10^{-003}	-7.160×10^{-004}, 1.061×10^{-003}	1.074×10^{-003}, -2.141×10^{-003}
2	-8.467×10^{-005}, 1.749×10^{-003}	-6.889×10^{-004}, 1.047×10^{-003}	6.027×10^{-004}, 6.955×10^{-004}
3	4.805×10^{-006}, 2.671×10^{-006}	-5.547×10^{-004}, 9.521×10^{-004}	5.566×10^{-004}, -9.621×10^{-004}
4	6.922×10^{-004}, -1.315×10^{-003}	-3.810×10^{-004}, 7.502×10^{-004}	1.076×10^{-003}, -2.076×10^{-003}
5	-6.687×10^{-005}, 2.689×10^{-003}	-3.529×10^{-004}, 7.097×10^{-004}	2.869×10^{-004}, 1.972×10^{-003}

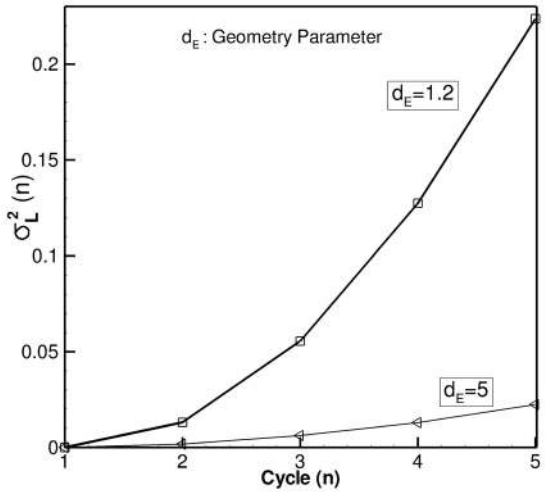

FIG. 9. Axial dispersion quantified by axial variance as a function of number of cycle. Subscript "L" is used for variance to indicate that the computation is carried out on the right vertical line of tracer shown in Figs. 8(a) and 8(b).

Having demonstrated typical advection patterns in the cavity, we present results of advection and drift in the mouth region. The visualization of advection of a line dye for which periodic boundary condition has been applied is shown in Fig. 7. The initial line is stretched into multiple cavities at $t/T=0.5$ as shown in Fig. 7(a). A large increase in length of the tracer during the positive half-cycle is noted. The dye is overlaid back on to a single cavity, resulting in an appearance of "layer structure" in the mouth as shown in Fig. 7(b). This is equivalent to the pattern of advection that can be expected when a dye is placed periodically in the alveolar mouth of all cavities in a physical scenario. Figure 7(c) shows the final shape of the dye after one complete advection cycle, exhibiting multiple folds [as opposed to a single fold of the right line dye inside the cavity in Fig. 5(a)]. The origin of folding is also attributable to steady streaming and will be discussed next in conjunction with the drift characteristics in the outer channel.

Advection in particle motion in the outer channel is studied by releasing two vertical lines of particles in the channel adjacent to the two corners of the cavity. The final shape of the tracer after one cycle shows the Lagrangian drift from its initial condition. Two values of $d_E=1.2$ and 5 are considered. As seen in Fig. 3, the upstream channel length is $d_E L$. By this specification, $d_E\to\infty$ is a model with a single cavity in an infinitely long channel, and $d_E=0$ is one where the channel is completely lined with grooves with no spacing in between. The drifts of these line tracers at end cycle calculated from Eq. (1) are shown in Figs. 8(a) and 8(b). Like Fig. 7(c), multiple folding patterns, hereafter referred to as "fold structure," are observed. The number of folds is higher for $d_E=1.2$ than for $d_E=5$. Multiple folds in the tracer clearly indicate that two particles initially located close to each other might overshoot or undershoot its initial location as observed inside the cavity [Fig. 5(a)], in the mouth region [Fig. 7(c)], and in the outer channel [Figs. 8(a) and 8(b)].

The advection characteristics of selected points (Lagrangian particles) 1, 2, 3, 4, and 5 marked in the dye for $d_E=5$ in Figs. 8(b) and 8(c) for $t/T=1$ and 0.5, respectively, are studied. The initial vertical line tracer on the right hand side is stretched over multiple cavities at end inspiration $t/T=0.5$. Only a section of the stretched tracer is shown in Fig. 8(c). Points 1 and 4 that consistently fall short of their initial positions (undershoot) after one cycle are always located near the left corner of the cavity at end inspiration. On the other hand, points 2 and 5 that overshoot their initial positions after one cycle are located at the right corner of the cavity at end inspiration. Point 3 which is almost traced back to its initial location is located over the channel at $t/T=0.5$. Table II shows that points 1 and 2 (or points 4 and 5) have nonzero y-component streaming velocities v_L of opposite signs, and the calculated $\boldsymbol{u}_L$, $\boldsymbol{u}_E$, and $\boldsymbol{u}_S$ satisfies $\boldsymbol{u}_L\approx\boldsymbol{u}_E+\boldsymbol{u}_S$ with an average error of 0.7%. Hence, it can be concluded that nonzero steady streaming velocities combined with pathlines of particles that traverse over multiple cavities (due to large K_C) result in the observed advection drift and folding patterns. The number of folds increases with increasing K_C (or decreasing cavity spacing). If a horizontal line dye is released in the mouth region as shown in Fig. 7, the resulting fold structure covers the mouth region as shown in Fig. 7(c). Unlike the fold structure formed at end cycle, the layer structure in Fig. 7(b) is irrelevant to mixing and is observed at end inspiration when a number of stretched tracers appear periodically over multiple cavities.

Axial dispersion in the channel caused by steady streaming shown in Fig. 8 is quantified by Eq. (3). The data at the end of first cycle are used as the reference initial condition to remove the effect of initial transient drift in the first cycle, which is usually greater than subsequent cycles. This is because of larger increase of dye interface from a line to folds in the first cycle while the fold pattern is retained in subsequent cycles. The variance shows an exponentially increasing trend with cycle number as seen in Fig. 9 for both cases $d_E=1.2$ and 5. Additional experiments were carried out and two important variables that alter the observed fold structure significantly were realized. These are the Keulegan–Carpenter number, K_C and geometrical ratio L/H (ratio of cavity length to channel height). Nevertheless, an elaborate parametrical study and identification of critical threshold values of these parameters is beyond the scope of this paper.

In summary, the relation between advection, stretch rate, steady streaming, and Lagrangian drift has been established in a simple 2D channel flow for Re=1 and $K_C=193$. It is shown that a mechanism that leads to large increase in dye interface length exists in a low-Re flow that arises due to streaming. With the physical insights gained from this case, we proceed to report the results in 3D acinar models. Unlike the 2D channel flow, all cases, except one, presented below consider uniform expansion and contraction of the 3D duct and alveolar walls.

B. Alveolar flow structure

The characteristics of the flows in Cases I and II are briefly described here. In the proximal generations, the main cavity flow typically consists of a recirculation near the

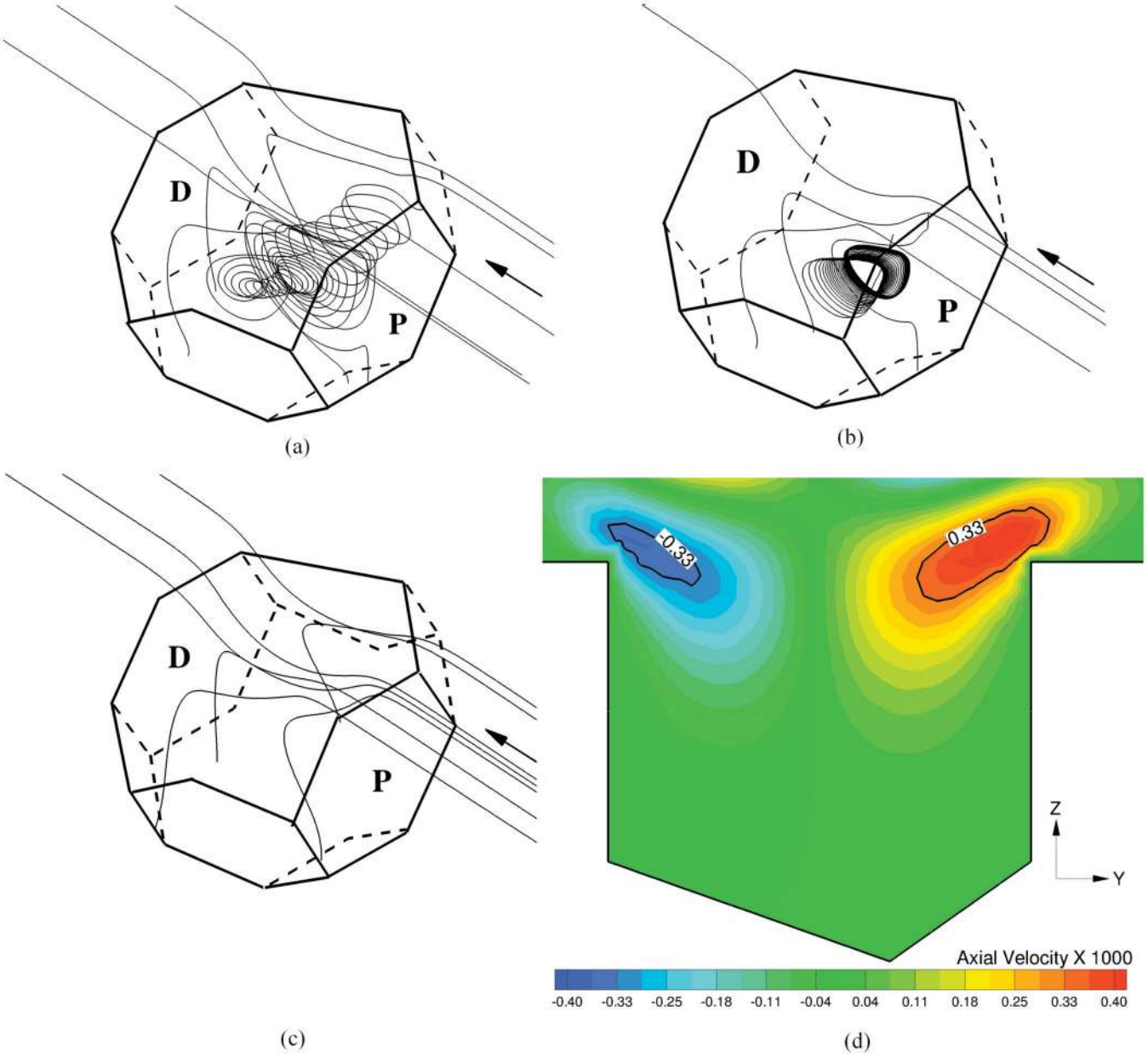

FIG. 10. (Color) 3D view of instantaneous stream-trace portrait near peak inspiration at $t/T=0.24$ within and over the alveolar cavity ALV for Case I (see Fig. 1) with (a) Re=2; $Q_A/Q_D=0.0024$, (b) Re=1; $Q_A/Q_D=0.0047$, (c) Re=0.52; $Q_A/Q_D=0.0095$. P, proximal wall; D, distal wall. (d) Contours of Eulerian mean axial (y-component) velocity in the y-z plane of the cavity ALV for Case I with Re=1.

proximal wall. The only nondiffusive interaction between the duct and the alveoli occurs through an entrainment region. The presence of such an entraining flow is a consequence of expansion and contraction of alveolar walls. Hence the fluid exchange to and from the alveoli occurs through a region located near the proximal wall corner.[18,26] An instantaneous portrait of stream-traces above and within the alveolus for Case I is given in Figs. 10(a)–10(c) for Re=2, 1, and 0.52, respectively. For flows with Re=2 and 1, a recirculation is present within the cavity near the proximal wall.[26] Figure 10(c) corresponds to a lower-Re flow where recirculation is absent. Also, for all $Re<0.52$ including Re=0.06 case which will be considered later, no recirculation is observed within the alveolus. The flow structure within an alveolus in Case II, in general is similar to Case I. However, due to the asymmetric arrangement of alveoli around the duct, alveolar units surrounding the duct are ventilated nonuniformly.

Since steady streaming plays an important role in mixing as demonstrated before with a 2D alveolated channel flow, Fig. 10(d) shows the contours of the steady streaming Eulerian mean axial (y-component) velocity in the y-z plane of an alveolus for Case I with Re=1 [refer to Fig. 1(d) for the location of the y-z plane]. The positive and negative streaming velocities are observed in the proximal (right) and distal (left) corners of the alveolus, exhibiting the same feature as the 2D rigid-channel case in spite of the 3D moving wall. For a given Re, the major difference from the rigid-wall case is that the magnitude of the streaming velocity in the

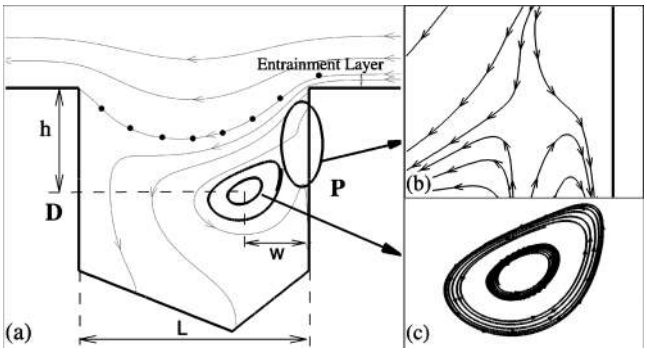

FIG. 11. (a) Stream-traces in the y-z plane of the alveolus ALV [see Fig. 1(d)] for Case I, Re=1 at $t/T=0.24$. The entrainment layer is denoted by a double-sided arrow, and its upper bound is delineated by the stream-trace marked with circles. P, proximal wall; D, distal wall. Enlarged view of: (b) a saddle point, (c) a center point (associated with recirculation). For a saddle point, $\mathrm{Im}(\lambda_1)=\mathrm{Im}(\lambda_2)=0$, $\mathrm{Real}(\lambda_1)\times\mathrm{Real}(\lambda_2)<0$; for a center point, $\mathrm{Real}(\lambda_1)=\mathrm{Real}(\lambda_2)=0$.

moving-wall case is slightly lower than that of the rigid-wall case and is more asymmetric, having greater positive streaming velocity than negative one. With increasing (decreasing) Re to 2 (0.52), the maximum Eulerian axial velocity increases (decreases) approximately by twofold.

C. Flow topology classification

Figure 11 illustrates the flow topology and associated critical points within the alveolus by showing the instantaneous stream-traces in the y-z plane of the alveolus "ALV" displayed in Fig. 1(d). The reasons for identifying critical points are twofold. First, a stagnation saddle point had been attributed before for chaotic mixing in the alveoli.[10,14,15,18] Second, the observed flow topology helps identify advection regions of interest for analysis in subsequent sections.

The flow topology can be classified by the first-order critical points of the flow in the y-z midplane. The type of critical points depends on the eigenvalues of the velocity gradient in the vicinity of a critical point.[38,39] The magnitude of fluid velocity vanishes at a critical point. The eigenvalues are computed from the characteristic equation $|[A]-\lambda[I]|=0$, where $[A]=A_{ij}=\partial u_i/\partial x_j$ is the Jacobian matrix based on the velocity gradient in the midplane and λs are eigenvalues, λ_1 and λ_2. The eigenvalues and the type of critical points for Case I, Re=2 and 1, are listed in Table III at time instants that roughly correspond to the maximum flow rate during inspiration and expiration. Two critical points are observed in Fig. 11. By definition, if both eigenvalues are real with at least one of them being negative, the critical point is a "saddle" point [see Fig. 11(b)]. If both eigenvalues are complex conjugates, the critical point is called a "center" [see Fig. 11(c)]. The center point is found at the center of the recirculation, whereas the saddle point is near the proximal wall. The presence of the saddle point is consistent with Refs. 14, 17, and 18 who also recognized its presence within the cavity. Tsuda *et al.* explained that such a saddle point arises from superposition of a main recirculating cavity flow and the radial flow generated by wall motion.[14]

As the critical point is in essence a stagnation point, the magnitude of velocity near the saddle point is relatively small. During expansion, the saddle point and recirculation are displaced deeper into the cavity. As shown in Fig. 11(b), a saddle point diverts streamlines that pass into it to different regions, thus leading to uncertainty. The nonzero real part of the eigenvalue of the center-like point depicts a spiral behavior. The change in sign between inspiration and expiration indicates the direction of this spiral. That is, the negative (positive) real part of the center-like spiral point implies that particles in its vicinity tend to move toward (away from) that point in a spiral fashion. Although the particles could move toward the spiral point from any direction, there is no guarantee that they would follow the same path in a reversible manner when moving away from it, resulting in uncertainty. Hence it was postulated that the presence of critical points might give rise to mixing in its neighborhood.

The entrainment region, a thin layer attached to the ductal wall, is also marked in Fig. 11. The stream-trace, which represents the upper bound of this layer, is overlaid with solid circles. This stream-trace is open to the channel on the proximal wall side, but is closed and attached to the distal wall, allowing advection of fluid into or out of the cavity. The presence of the entrainment region restricts the recirculation eddy to the right hand side of the cavity close to the proximal wall, and forms a saddle point where recirculating flow interacts with entrained flow and radial flow induced by wall motion. In contrast, for the rigid-wall case, like the 2D channel flow shown in Fig. 3(b), a separation line is formed at the mouth region to separate ductal flow from cavity flow and the recirculation is located approximately at the center of the cavity.

D. Tracer advection and deformation

In this section, we investigate the Lagrangian drift that arises in tracer transport in an alveolus. For the tracer advection experiments below we shall consider the alveolus ALV marked in Fig. 1(a). For clarity, different 3D views of the alveolus are provided in Figs. 1(c) and 1(d). A cross-shaped dye is introduced within the cavity and its deformation is monitored for ten cycles to assess the effect of recirculation on mixing. A visualization of the final shape of the dye for three different flow conditions is shown in Fig. 12. The four arms of the dye are numbered, aiming to observe advection

TABLE III. Critical points in the flow.

				Location	
Re	Time	Eigenvalues	Type	w/L	h/L
Re=2	0.48π	$0.203\pm5.63i$	Spiral	0.366	0.477
		15.194, −0.98	Saddle	0.03	0.187
	1.52π	$-0.2054\pm5.6i$	Spiral	0.38	0.482
		0.987, −15.83	Saddle	0.032	0.192
Re=1	0.48π	$0.03\pm3.33i$	Center	0.2665	0.447
		2.542, −8.099	Saddle	0.046	0.207
	1.52π	$-0.036\pm3.3i$	Center	0.267	0.45
		8.351, −2.74	Saddle	0.045	0.21

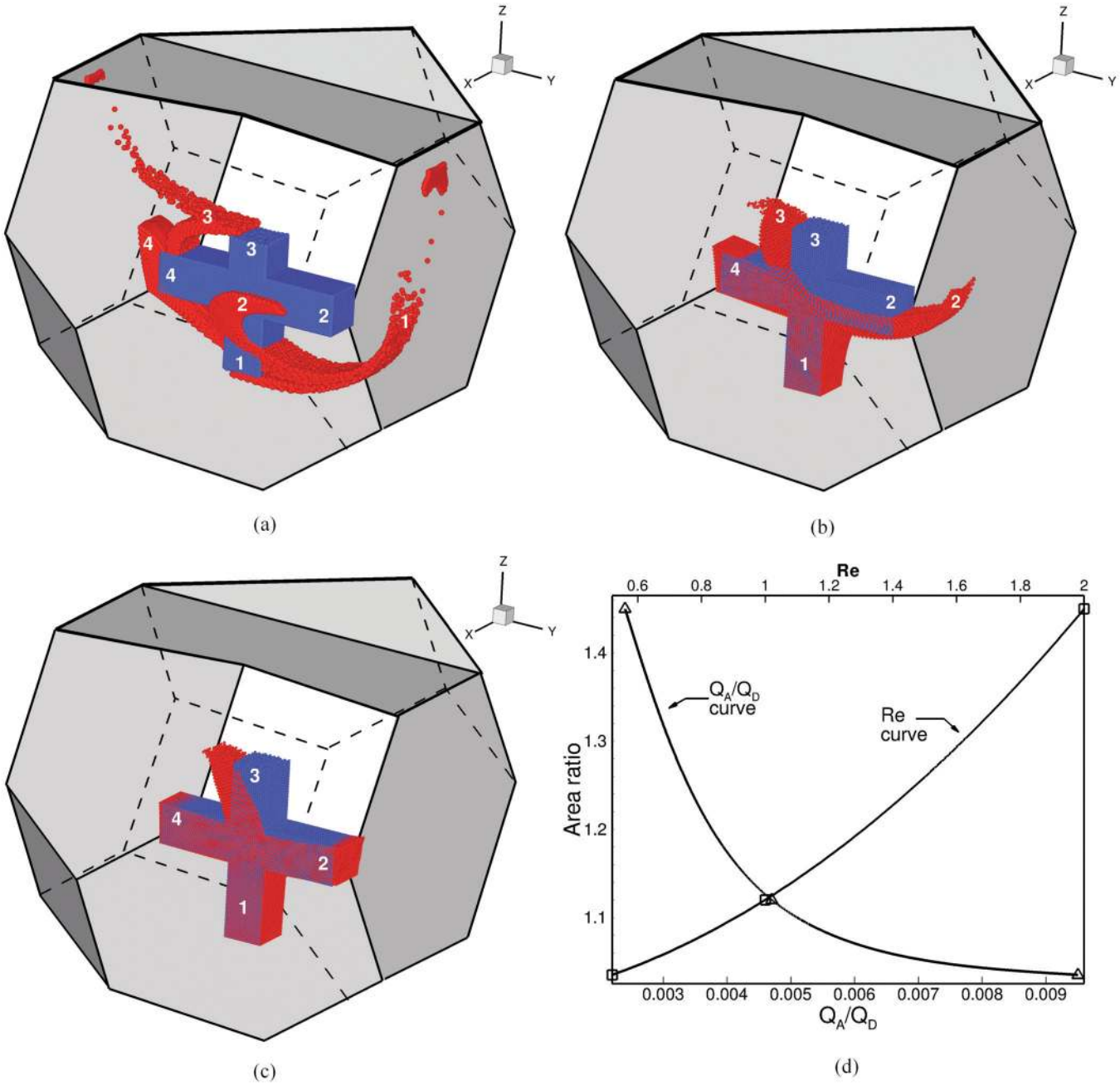

FIG. 12. (Color) Advection patterns for an initial cross-shaped dye within the cavity ALV of Case I for (a) Re=2; Q_A/Q_D=0.0024, (b) Re=1; Q_A/Q_D =0.0047, and (c) Re=0.52; Q_A/Q_D=0.0095 after ten periods of breathing. The blue dye is the initial shape of the dye and the red dye is the deformed shape after advection. (d) Correlation of red-blue interface area ratio with Q_A/Q_D and Re.

in four regions of the cavity. The dye experiences an increase in the interface area due to the alveolar flow: ~45% increase for Re=2(Q_A/Q_D=0.0024), ~12% for Re=1(Q_A/Q_D =0.0047) and ~3.5% for Re=0.52(Q_A/Q_D=0.0095). Similar to the observed folding phenomena in the 2D case of Fig. 6, a stretch of material into the proximal corner is observed due to steady streaming. Again indicative of the Re effects, the drift is more pronounced for Re=2 than Re=1 and for Re =1 than Re=0.52. In particular, at Re=2, blue arm #1 is folded and stretched toward the upper proximal wall, and arm #3 near the mouth region is also highly stretched. At Re=1, the recirculation zone is reduced (see Figs. 10 and 11), and thus only stretch of arm #2 is evident. Arm #3 still experiences stretching because of its proximity to the mouth region. At Re=0.52, the recirculation is absent (see Fig. 10) and only the stretch of arm #3 seems significant. The increase in the red-blue interface area ratio is correlated as roughly quadratic with increasing Re [see Fig. 12(d)]. It is also useful to plot the ratio as a function of the flow ratio Q_A/Q_D defined earlier. The interface area increases almost exponentially with decreasing values of Q_A/Q_D.

Previously the advection and deformation of tracers inside the cavity are examined by a cross-shaped dye. Next, a planar tracer is advected for one full cycle. The tracer is

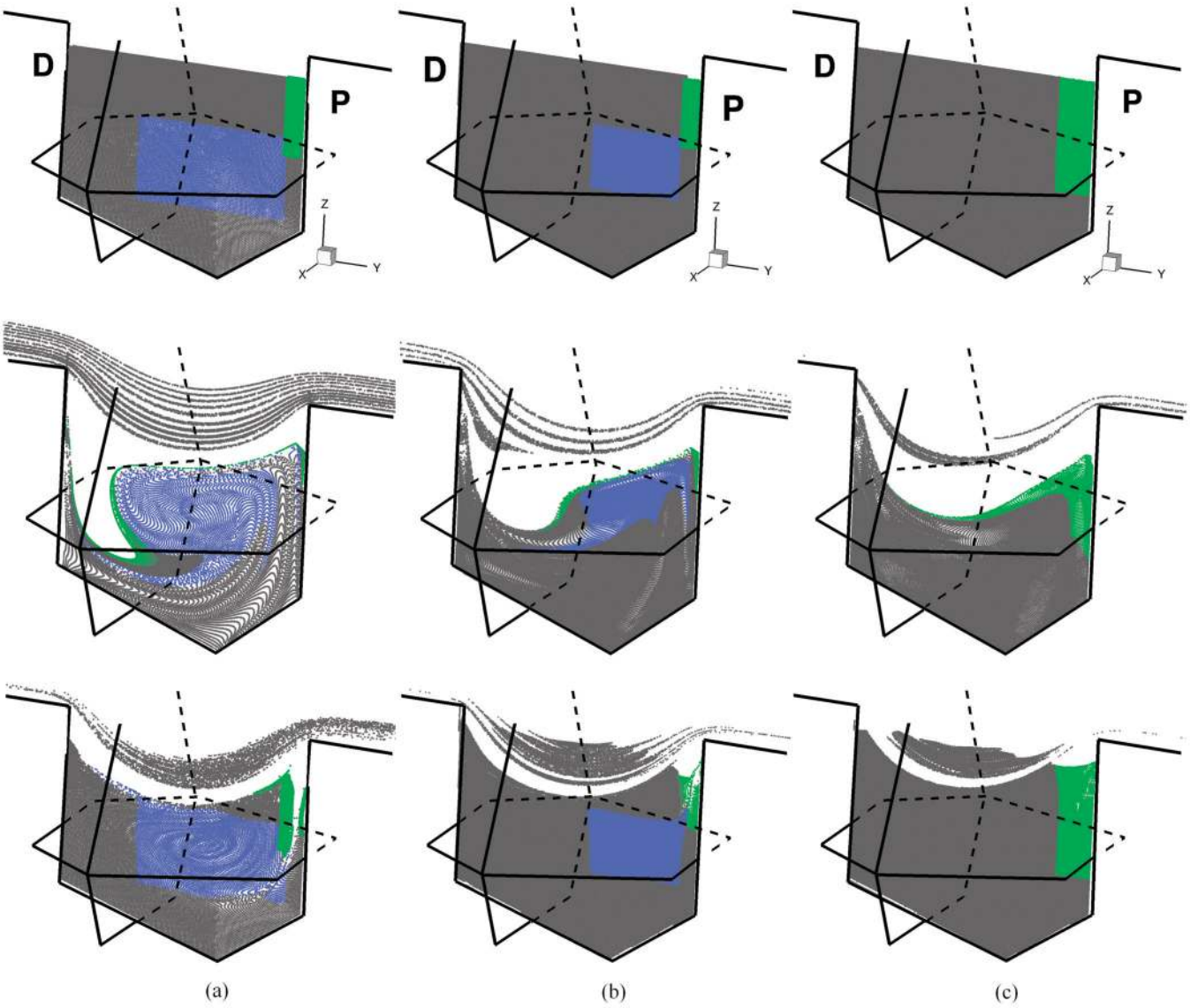

FIG. 13. (Color) Material advection in the y-z plane of the cavity ALV of Case I [see Fig. 1(d)] with (a) Re=2; Q_A/Q_D=0.0024 (b) Re=1; Q_A/Q_D =0.0047, (c) Re=0.52; Q_A/Q_D=0.0095 at t/T=0 (top panel), 0.5 (middle panel), and 1.0 (bottom panel). P, proximal wall; D, distal wall. The blue (green) dye in (a) and (b) covers a center-like spiral point (a stagnation saddle point). There is no critical point in (c) due to very low-Re.

constructed using ~20 000 particles and placed initially in the y-z plane shown in Fig. 1(d). The advection is carried out in a complete 3D sense utilizing all the three velocity components. Figure 13 shows advection characteristics in the midplane for Case I, which are of particular interest for reasons discussed in Sec. III A in association with steady streaming. For studying the characteristics of deformation within the alveolus, the advection pattern in strategic regions within the planar tracer are separately followed. These regions are depicted by different colors and illustrated in Fig. 13. The blue tracer, on average, covers the region inside the cavity where recirculation (in the neighborhood of the center point) is observed. Mixing in the neighborhood of the proximal region (associated with the saddle point) within the alveolus is identified using the green tracer. As observed in Fig. 11, the midplane contains a saddle point near the proximal cavity wall. The rest of the cavity is colored in gray.

The layered appearance of the gray tracer at end inspiration, as seen in the middle panel of Figs. 13(a)–13(c), is a visualization of traverse of the tracer in multiple alveolar units and has already been discussed in conjunction with Fig. 7(b). Because the axial distance traveled is greater for Re =2 than Re=1, and for Re=1 than Re=0.52, the number of layers observed is higher in Fig. 13(a) than Fig. 13(b), and in Fig. 13(b) than Fig. 13(c).

Mixing within the alveolus is visualized by the deformation of the blue and green regions. For Re=2 the blue region at end inspiration t/T=0.5 is stretched in a manner similar to the 2D channel case shown in Fig. 6(b). Recall that in the presence of alveolar and ductal wall expansion, the recirculation eddy is shifted toward the proximal wall to accommodate the entrained flow. Therefore, the blue dye can hardly reach the distal wall of the cavity. At end expiration (i.e., end cycle, t/T=1), the fold structure similar to the 2D case in Fig. 6(c) is observed. The fold structure extends further up to the green tracer region. At the mouth region, the fold struc-

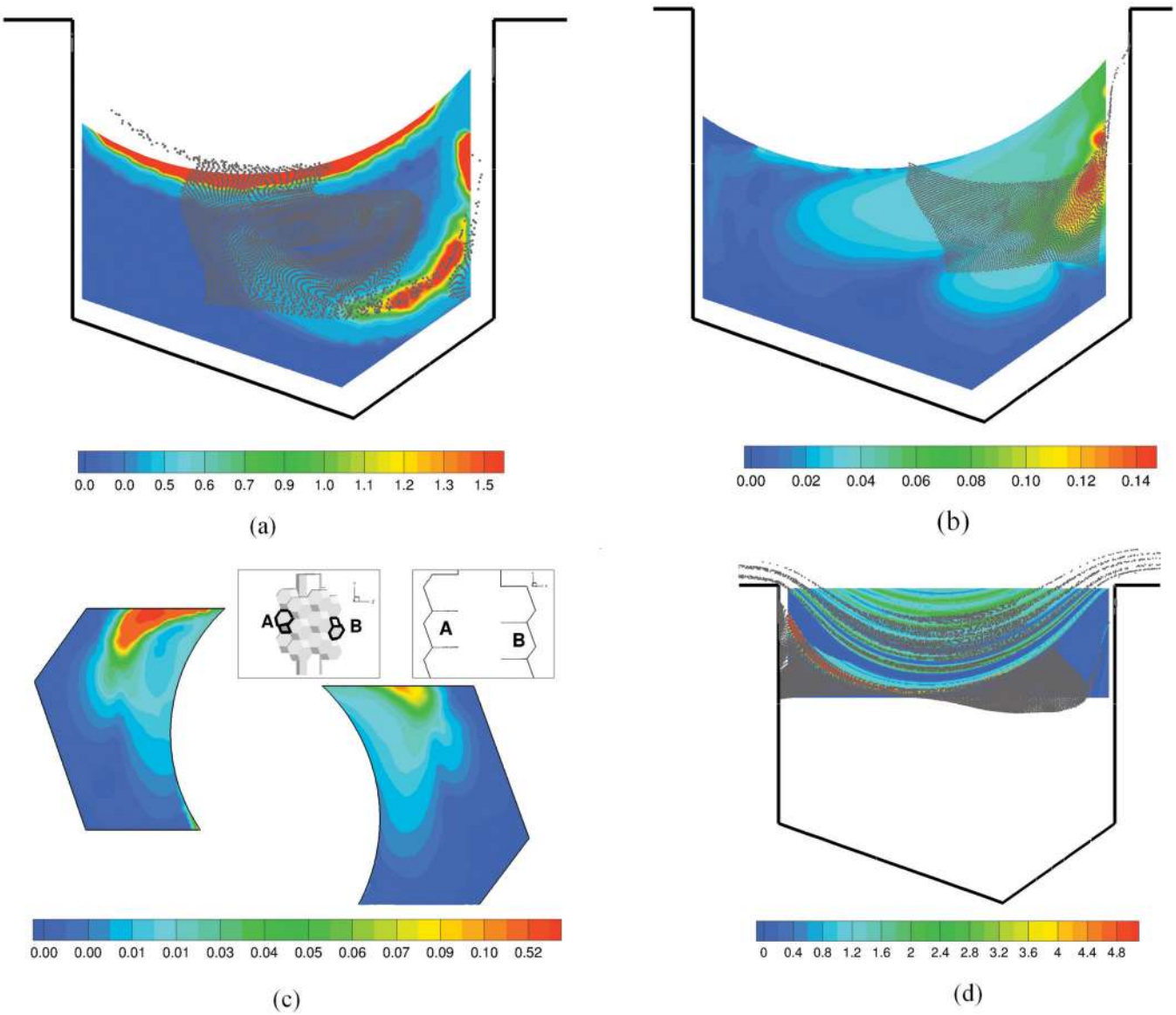

FIG. 14. (Color) Maps of stretch rate (s_l) after five cycles in the y-z plane of the alveolar cavity for: (a) Case I, Re=2.0, Q_A/Q_D=0.0024, (b) Case I, Re =1, Q_A/Q_D=0.0047, (c) Case II, Re=1; Q_A/Q_D=0.0047, (d) in the mouth region of Case I, Re=1. For Case I the alveolus ALV in Fig. 1(a) is examined. For Case II two alveoli marked by "A" and "B" in the two inserts of (c) are examined with the left one A closer to the ductal entrance E. The distributions of particles covering the recirculation region of Case I [the blue dyes in Figs. 13(a) and 13(b)] after five cycles are overlaid with stretch rate maps in (a) and (b), and the distribution of particles in the mouth region is overlaid in (d).

ture is also formed at $t/T=1$. The particle distribution at the mouth region in association with folds appears to shift to the proximal wall side, closer to the entrainment layer, especially at Re=2. The appearance of fold structure implies mixing which will be quantified later. For Re=1, the blue tracer region is smaller than that of Re=2 because the size of the recirculation eddy reduces in size. A smaller recirculation yields smaller stretching of the blue tracer at peak inspiration [see Fig. 13(b), middle panel]. The fold structures inside the cavity and at the mouth region are also observed in Fig. 13(b), bottom panel. For Re=0.52, there is no recirculation, nor a stagnation saddle point. The green tracer is almost restored to its original shape as shown in Fig. 13(c), bottom panel. Nonetheless, the fold structure at the mouth region is still observed. We also performed advection experiment for tracers released within the cavity for Re=0.06 case mentioned earlier in Sec. III B. The net displacement of particles within the cavity after five cycles is observed to be three orders-of-magnitude smaller than observed in the Re=0.52 case.

E. Stretch rate map

The spatial distribution of stretch rate, also known as a "stretch rate map," represents stretching histories of Lagrangian particles seeded over an area and computed by Eq. (2). First, stretch rate within the cavity is considered. Figure 14 depicts slices of stretch rate inside the alveolus in the y-z plane for Cases I and II. Relatively high-stretch rate zones are limited to localized regions within the alveolus. In Fig.

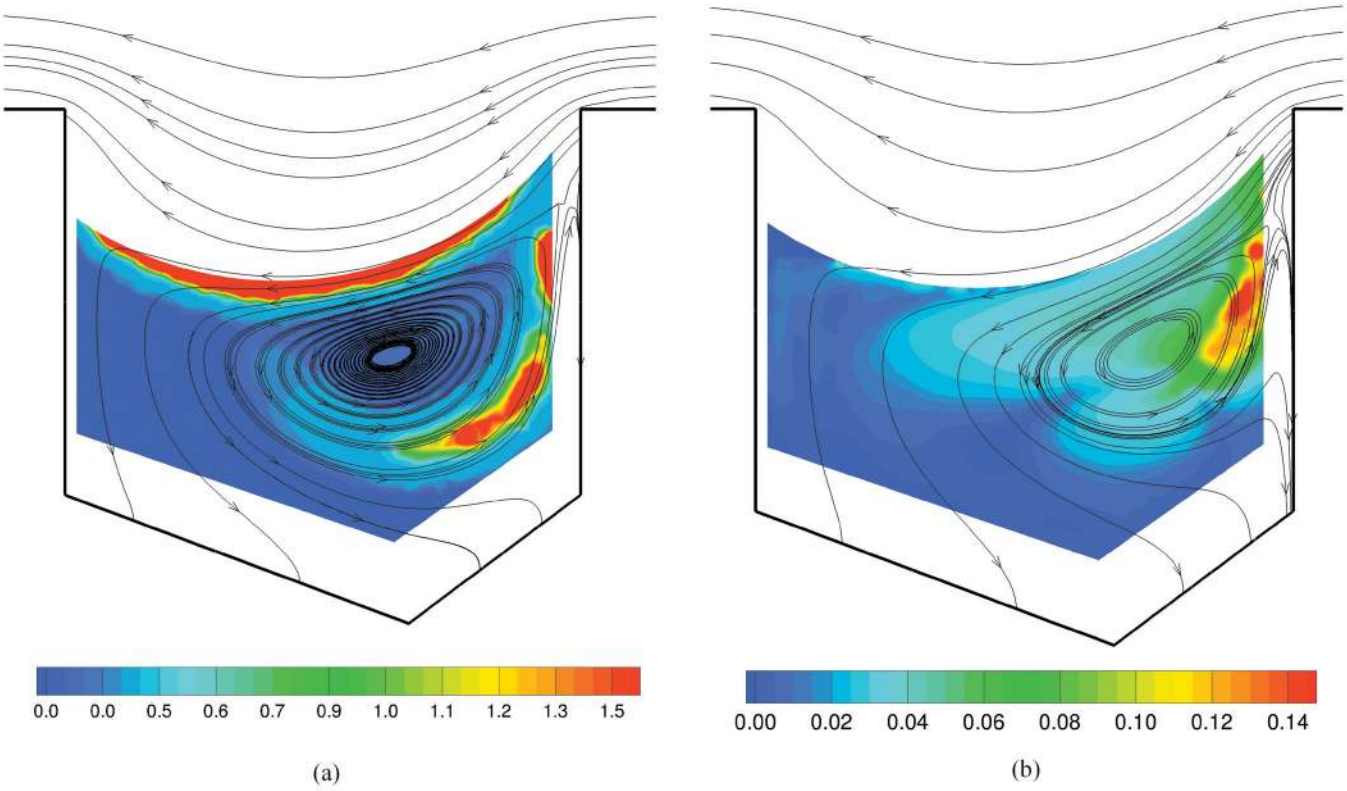

FIG. 15. (Color) Stream-traces near peak inspiration at $t/T=0.24$ overlaid with stretch rate map for Case I with Re=: (a) 2, (b) 1.

14(a), a tongue of high stretching surrounds a region of almost zero stretching, resembling the fold structure inside the cavity shown in Figs. 6(c) and 6(d). The high-stretch-rate regions near the proximal wall in Figs. 14(a) and 14(b) roughly correspond to the spreading of the blue tracer toward the proximal wall in Figs. 13(a) and 13(b). The distributions of particle tracer after five cycles are superimposed on the stretch rate maps in Figs. 14(a) and 14(b), confirming the physical correlation between stretch rate and tracer deformation. The shape and length of the tongue of this high-stretch region are dependent on the size and shape of recirculation and its advection of particles to the steady streaming zone as discussed in Sec. III A. When Re=2, the size of recirculation is larger. Hence the high-stretch tongue is larger in length, extending into the cavity. On the other hand, when Re=1, the size of recirculation is small and is more shifted toward the proximal wall, resulting in the observed high-stretch region in Fig. 14(b). The stretch rate map for two alveolar units [marked in Fig. 1(b)] for Case II with Re=1 are shown in Fig. 14(c). As in Case I, the high-stretch rate is observed near the proximal region. Although both Cases I and II in Figs. 14(b) and 14(c) have the same Re at the ductal entrance, more alveolation in Case II enhances stretch rate by ~4 times. In addition, the left alveolus has higher stretch rate than the right one because of the geometrical effect.

In Fig. 14(d), the stretch rate map at the mouth region of Case I with Re=1 is overlaid with the tracer distribution after five cycles. The high stretch-rate distribution is correlated well with the tracer distribution. Transport in this region represents the nature of duct-alveoli interaction. The stretch rate map in the alveolar mouth region is of higher complexity, stratified in appearance with alternating higher and lower values of contours, resembling the fold structure shown in Fig. 7(c) due to steady streaming. It is noted that the stretch rate at the mouth region is an order-of-magnitude higher than inside the cavity, suggesting that stretching and folding of dye interface in the mouth region is much more effective than inside the cavity.

To correlate the high-stretch rate region (effective mixing region) inside the cavity with the flow topology (e.g., center and saddle critical points, recirculation, and entrainment), Fig. 15 overlays the stream-traces near peak inspiration with the stretch rate map. This suggests that the high stretch rate (effective mixing) takes places along the periphery of the recirculation and at the mouth region in association with entrained flow and it does not necessarily coincide with the saddle point. The center point of the recirculation at Re=2 appears to contribute little to mixing.

The time-averaged stretch rates shown in Fig. 15 can be averaged over the entire flow field to get a single-value volume-averaged stretch rate at various conditions for comparison. The volume-averaged stretch rate thus obtained gives the mixing rate solely determined by the kinematics of the flow, and is referred to as kinematic mixing rate. Figure 16 plots the variation of mixing rate with Q_A/Q_D and Re for the cases considered. The mixing rate is approximately equivalent to the separation rate of adjacent array of particles.[29] The stretch rate in Eq. (2) is a logarithmic rate. Hence, if the average stretch rate is "s_l" after time "nT," the approximate separation between particles roughly increases

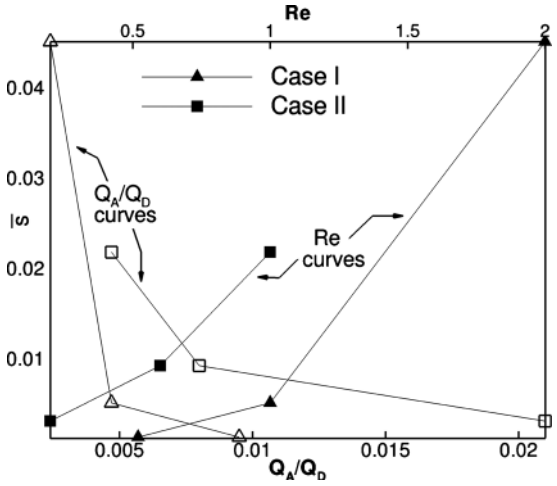

FIG. 16. Effects of Q_A/Q_D and Re on kinematic mixing rate.

by $100(e^{s_l \times nT}-1)\%$. The mixing rate for Case I is ~0.04 at Re=2 and ~0.005 for Re=1. The average separation between particles in the flow roughly increases by ~65% when Re=2(Q_A/Q_D=0.0024), and by only ~7% for Re =1(Q_A/Q_D=0.0047). The mixing rate is ~0.02 in Case II for Re=1(Q_A/Q_D=0.0047) and decreases to ~0.009 for Re =0.6(Q_A/Q_D=0.008). As illustrated in Fig. 12(d), a rapid reduction in mixing rate is evident for both Cases I and II as Re decreases and Q_A/Q_D increases down the acinar tree.

F. Dispersion in alveolated duct

While the previous section focuses on convective displacement of particles within the alveolus and at the alveolar mouth region, this section is primarily concerned with axial dispersion in the ductal region of the acinar airways. The streaming mechanism governing axial spreading of a dye in a 2D alveolated channel is analyzed in Sec. III A. Based on the definition of d_E in Sec. III A, d_E=1.2 for Case I and d_E=0 for Case II. For the 3D geometry considered here, it is not surprising that a similar advection pattern would be observed. But the motion of the wall introduces some changes to the advection characteristics of particles close to the cavity. Unlike the rigid-wall case, a fraction of particles from the duct and from the alveolar mouth penetrate deeper into the cavity during inspiration. These particles may not return back to its original location. Also, the fraction of the particles entering the alveoli is small (observed to be less than ~2% when Re=1). The net dispersion of particles in the duct studied in this section is hence primarily attributed to the axial spreading mechanism. For illustrative purposes, the advection of a planar dye released in the duct near the proximal wall is displayed in Fig. 17(a). Similar to the 2D-fold structure shown in Fig. 8, a 3D-fold structure in the dye after one advection cycle is observed. This drift is the 3D equivalent of axial spreading caused by steady streaming as discussed before. We now proceed to quantify the observed dispersion in the axial direction.

A bolus consisting of ~40 000 particles are released in the entrance of the alveolar duct and advected through multiple cycles. Dispersion of the bolus is calculated by Eq. (3).

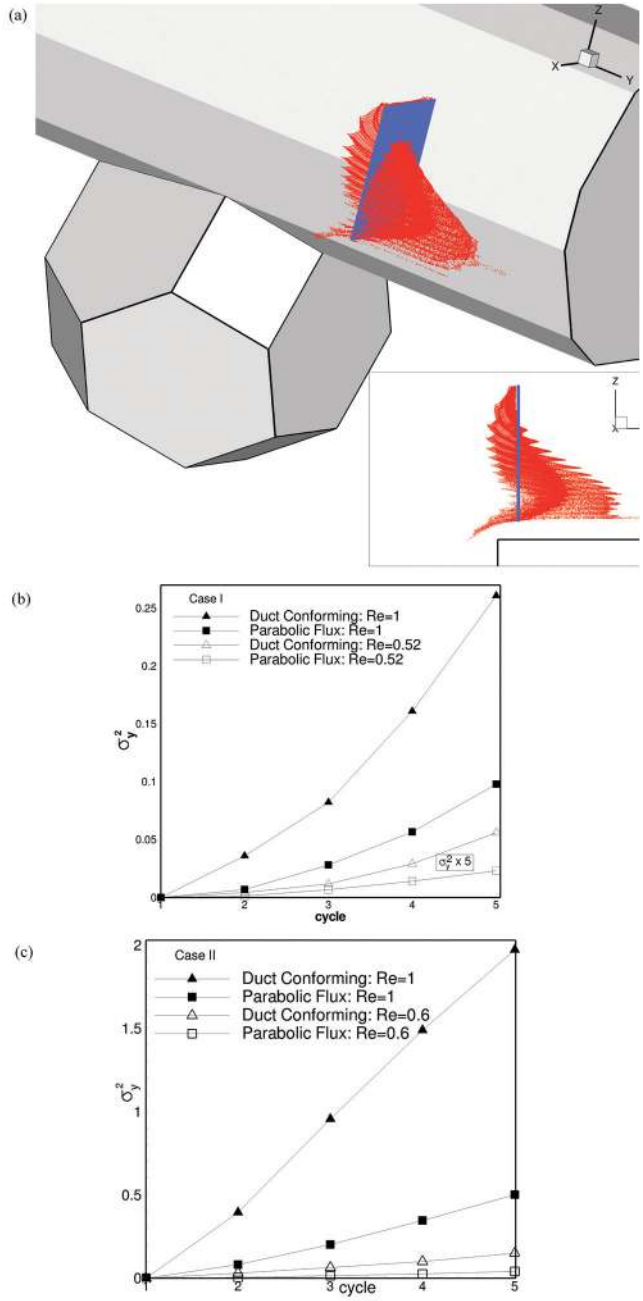

FIG. 17. (Color) (a) Drift of an initial rectangular-plane dye (blue) in the duct for Case I, Re=1. The final shape of the dye after one cycle is in red. The insert shows the same when looking into the *x*-plane. [(b) and (c)] Axial variance vs cycle number in Case I and Case II, respectively. The variances for Re=0.52 have been amplified by five times.

The particle location at the first cycle is treated as the base state in Eq. (3) to remove the initial transient effect. Two different initial distributions of bolus with the same particle flux density, number/μm^3, are considered: (1) a parabolic distribution and (2) a uniform particle flux distribution. Both distributions are introduced at the entrance of the alveolar duct. Figures 17(b) and 17(c) show the evolution of axial variance for Case I and Case II at different Q_A/Q_D and Re. There exists significant difference in the estimated dispersion for the two initial distributions. For example, when Re=1, about threefold increase for Case I and fourfold increase for

Case II are observed at the end of five time periods as shown in Figs. 17(b) and 17(c) clearly illustrating the accelerated dispersion due to streaming. The extent of the axial spread of the tracer increases as we move away from the centerline as evident in Fig. 17(a). This can also be seen in Fig. 8(b) for the 2D case, where the drifts of points 1 and 2 are smaller than those of points 4 and 5. In an initial parabolic distribution, the concentration of particles decreases away from the duct centerline. Hence, dispersion of particles in a region of higher particle concentration, which is near the ductal center, is less. The importance of geometry on axial dispersion can be related back to the streaming mechanism discussed in Sec. III A. It is recollected that the variances in Fig. 9 for the two cases of d_E differed significantly. Hence, it can be concluded that geometry plays a crucial role in the accurate estimation of dispersion in acinar airways.

The effect of Re on the resulting dispersion is also significant. For example, variance in Cases I and II drops by one order-of-magnitude when Re is halved, for both initial flux distributions.

IV. DISCUSSION AND CONCLUSIONS

Alveolar flow is a time-periodic low-Re flow phenomenon occurring in open cavities. Cavities, in general, are stagnant pockets, which show weak transport unless modified by some form of temporal perturbation.[7] The extent of mixing achieved by low-Re acinar flow, under normal breathing conditions, reversible wall motion and perfectly sinusoidal ductal flow is the topic of the current investigation. Improved understanding of acinar mixing helps in better prediction of particle transport, dispersion, and the ultimate deposition of fine particles deep in the lung. For example, bolus dispersion studies cannot individually simulate flow and transport in each region of the acinus, due entirely to its complexity. Mixing factor is a term commonly used in these studies to denote the fraction of particles transported from the inhaled to residual air in the alveolar region. This factor is mostly empirical and accounts for the flow-induced mixing. Its importance can be quickly realized from the observation that 0.5–1 μm particles show an order-of-magnitude difference in deposition fraction between cases of zero and total mixing.[40–42] Hence, obtaining average mixing estimates is a main objective of this work.

The mixing measures rely on the estimation of particle motion due to nonzero inertia and geometry. The important contributions of this paper may be summarized as follows. Acinar flows belong to a unique category of low-Re high K_C oscillatory flows. An open cavity geometry is used as a simple prototype for alveoli, to observe a Lagrangian drift and hence an increase in interface length. This is shown to result in advective mixing studied from different viewpoints—mixing in the duct, mixing within the alveolus and their interaction. The origin of the Lagrangian drift in these regions can all be explained by the steady streaming phenomenon in an oscillatory flow. Using this basic understanding of the mechanism, estimates such as tracer deformation, stretching, and dispersion are used to quantify this advective mixing in 3D acinar models. Critical points in the flow are also identified within the cavity based on an analysis of eigenvalues computed from the velocity gradient in the midplane. However, they are not physically correlated with regions of high stretch rate.

The steady streaming mechanism also accounts for considerable axial dispersion in alveolated channels and ducts. Such a drift mechanism exists due to alveolation even in the absence of wall motion. Previously, Henry *et al.* observed a "finger-like" stretch of the dye interface in their multicell alveolar model.[18] Their model was one of expanding and contracting during one cycle. The exact origins of this finger-like structure in the tracer advection were not discussed. Also, it was reported that the formation of this structure in the duct was associated with the presence (or absence) of recirculation. On the contrary, our analysis and results clearly indicate that the presence of recirculation inside the cavity have no bearing on the observed drift in the dye. Instead, the observed drift in tracer transport is of hydrodynamic origin and can be directly correlated with steady streaming. Such low-Re hydrodynamic streaming-induced phenomenon has been recorded earlier in different environments. For example, Flekkøy *et al.* observed similar "pinch" dispersion of tracer in a Hele–Shaw cell in the presence of an obstacle.[36] More recently, Larrieu *et al.* observed Lagrangian drift for oscillatory flow over a wavy wall due to streaming.[34] Wang and Ottino observed that increasing K_C increases disorder in tracer motion in a lid-driven cavity flow.[43] The present finding is unique to low-Re open cavity flows directly applicable to dispersion in acinar airways with a large displacement parameter, K_C.

We have also supplemented our mixing study with stretching analysis. Haber *et al.* investigated flow inside a hemispherical cavity.[17] In their study of mixing, stretching was computed using $(\underline{D}:\underline{D})^{1/2}$ where the velocity gradient tensor $\underline{D}$ was calculated through advection of an array of particles, although they did not arrive at a parametrical mixing estimate. The stretch rate map for Case I agrees qualitatively with those of Haber *et al.*, showing higher stretch rate near the proximal wall.[17]

The conclusions presented thus far have important physiological implications with respect to the fate of inhaled pharmaceutical and pollutant particle clouds in the acinus. In the adult human lung, less than ~13% of alveoli originate from bronchioles in the first three acinar generations, while almost ~87% originate from alveolar ducts and sacs.[8] Under normal breathing conditions, Re is typically 0.6–1.0, for the first few acinar generations. Hence, when one neglects gravitational and diffusional mechanisms, advective mixing of an inhaled bolus could originate in respiratory bronchioles (and more significantly for $\mathrm{Re}>1$) and may extend up to the beginning of alveolar ducts. In the later generations (when $\mathrm{Re}\leq 0.52$), the flow-induced dispersion and the resulting convective mixing inside the cavity are negligible. But, the unique combination of low-Re, high-K_C oscillatory shear flow in the presence of an alveolar cavity causes nonnegligible dispersion in the alveolar duct. The low-Re flow in distal generations could still achieve effective mixing through other mechanisms like parent-daughter branching,

TABLE IV. Mesh sensitivity test.

Mesh case	Coarse mesh	Fine mesh	Very fine mesh
Number of elements	11 000	25 200	85 500
Element size near the corner (Δ/L)	0.015 66	0.0087	0.004 475
Maximum (axial) $\boldsymbol{u}_E$ magnitude $\times$ 1000	1.367	1.377	1.38

hysteresis in wall motion and ductal-alveolar flow phase lag[17] and is a topic of future work.

The extrapolation of the mixing measures and correlations to the entire acinar region of the lung should be done with caution and the predictions may not completely hold true in the lung in-vivo. Just like the upper airways, the acinus also consists of bifurcations or branching causing a progressive reduction in Re along the acinar tree. Although the low-Re flow quickly assumes a parabolic velocity profile in the duct space at the end of one branch before entering the daughter branch, the role of the bifurcation on mixing is not completely known. The present approach cannot capture this effect as it requires an elaborate geometry of the entire acinus although certain efforts in this direction have been attempted recently.[11,12] Harrington *et al.* and Sznitman *et al.* have performed computations in a bifurcation model at low-Re.[11,12] But none of these works have performed advective mixing analysis or dispersion estimates. Recent efforts have used high-resolution Computed Tomography (CT) based models of alveolar sac to perform simulation.[44] Apart from the geometrical variations, asymmetry effects, like waveform differences between inspiration and expiration and hysteresis in wall motion,[17] are yet to be investigated.

ACKNOWLEDGMENTS

This work was supported in part by NIH Grant Nos. R01-HL-094315, R01-EB-005823, R01-HL-064368, and S10-RR-022421. The authors also thank TeraGrid via the Texas Advanced Computing Center for computer time. The authors sincerely thank Dr. Yong Kweon Suh for his invaluable comments on our manuscript and helping us clarify various terminologies. We thank Dr. Norman Riley for helpful discussions and clarifications.

APPENDIX A: VALIDATION OF STOKES DRIFT

Equation (7) for the Eulerian mean and Stokes drift velocities is validated with a progressive-wave problem which has an analytical solution. Consider a 2D progressive wave having a velocity profile of $\boldsymbol{u}=U(y)\sin(\lambda x-\omega t)\boldsymbol{i}+V(y)\cos(\lambda x-\omega t)\boldsymbol{j}$ with $U(y)$ and $V(y)$ satisfying continuity $\lambda U+dV/dy=0$. Here λ is the wavenumber and ω is the wave frequency, and $\boldsymbol{i}$ and $\boldsymbol{j}$ are unit vectors in the respective x and y directions. For this case, the Eulerian mean velocity $\boldsymbol{u}_E$ is zero and the Stokes drift velocity reads $\boldsymbol{u}_S=d^2(V^2/4\omega\lambda)/dy^2\boldsymbol{i}$. The set of parameters $T=10$, $\lambda=2\pi/16$, and $U=0.02$ are purposely chosen so that the analytical Stokes drift velocity $\boldsymbol{u}_S=\lambda U^2/2\omega\boldsymbol{i}=1.25\times10^{-04}\ \boldsymbol{i}$ is of the same order-of-magnitude as those in the open-cavity flows presented in Sec. III A. Our numerical advection procedure and the formulation given in Sec. II A and Eq. (7) predict a Stokes drift velocity within 0.5% of this analytical value.

APPENDIX B: MESH SENSITIVITY TEST

For the 2D open cavity flow at Re=1 considered in Sec. III A, the flow solution is computed in three different meshes. The mesh details are given in Table IV. As the mesh is unstructured, the size of the closest node to the cavity corner is reported. The Eulerian mean velocity $\boldsymbol{u}_E$ is computed. The peak of the Eulerian mean is reported at the same location near the corner for all the three cases. The percentage error between the fine mesh and the very fine mesh is $\sim$0.2%.

[1] H. Aref, "Stirring by chaotic advection," J. Fluid Mech. **143**, 1 (1984).
[2] W.-L. Chien, H. Rising, and J. M. Ottino, "Laminar mixing and chaotic mixing in several cavity flows," J. Fluid Mech. **170**, 355 (1986).
[3] P. D. Swanson and O. J. M. Ottino, "A comparative and experimental study of chaotic mixing of viscous fluids," J. Fluid Mech. **213**, 227 (1990).
[4] S. C. Jana and J. M. Ottino, "Chaos-enhanced transport in cellular flows," Philos. Trans. R. Soc. London, Ser. A **338**, 519 (1992).
[5] S. C. Jana, G. Metcalfe, and J. M. Ottino, "Experimental and computational studies of mixing in complex Stokes flows: The vortex mixing flow and multicellular cavity flows," J. Fluid Mech. **269**, 199 (1994).
[6] P. D. Anderson, O. S. Galaktionov, G. W. M. Peters, F. N. Van De Vosse, and H. E. H. Meijer, "Analysis of mixing in three-dimensional time-periodic cavity flows," J. Fluid Mech. **386**, 149 (1999).
[7] M. Horner, G. Metcalfe, S. Wiggins, and J. M. Ottino, "Transport enhancement mechanism in open cavities," J. Fluid Mech. **452**, 199 (2002).
[8] B. Haefeli-Bleuer and E. R. Weibel, "Morphometry of the human pulmonary acinus," Anat. Rec. **220**, 401 (1988).
[9] E. R. Weibel, B. Sapoval, and M. Filoche, "Design of peripheral airways for efficient gas exchange," Respir. Physiol. Neurbiol. **148**, 3 (2005).
[10] A. Tsuda, F. S. Henry, and J. P. Butler, "Gas and aerosol mixing in the acinus," Respir. Physiol. Neurbiol. **163**, 139 (2008).
[11] L. Harrington, G. K. Prisk, and C. Darquenne, "Importance of the bifurcation zone and branch orientation in simulated aerosol deposition in the alveolar zone of the human lung," J. Aerosol Sci. **37**, 37 (2006).
[12] J. Sznitman, T. Heimsch, J. H. Wildhaber, A. Tsuda, and T. Rosgen, "Respiratory flow phenomena and gravitational deposition in a three-dimensional space-filling model of the pulmonary acinar tree," J. Biomech. Eng. **131**, 031010 (2009).
[13] J. Heyder, J. D. Blanchard, H. A. Feldman, and J. D. Brian, "Convective mixing in human respiratory tract: Estimates with aerosol boli," J. Appl. Physiol. **64**, 1273 (1988).
[14] A. Tsuda, F. S. Henry, and J. P. Butler, "Chaotic mixing of alveolated duct flow in rhythmically expanding pulmonary acinus," J. Appl. Physiol. **79**, 1055 (1995).
[15] A. Tsuda, R. A. Rogers, P. E. Hydon, and J. P. Butler, "Chaotic mixing deep in the lung," Proc. Natl. Acad. Sci. U.S.A. **99**, 10173 (2002).
[16] J. P. Butler and A. Tsuda, "Effect of convective stretching and folding on aerosol mixing deep in the lung, assessed by approximate entropy," J. Appl. Physiol. **83**, 800 (1997).
[17] S. Haber, J. P. Butler, H. Brenner, I. Emanuel, and A. Tsuda, "Shear flow over a self-similar expanding pulmonary alveolus during rhythmical breathing," J. Fluid Mech. **405**, 243 (2000).
[18] F. S. Henry, J. P. Butler, and A. Tsuda, "Kinematically irreversible acinar flow: A departure from classical dispersive aerosol transport theories," J.

Appl. Physiol. **92**, 835 (2002).
[19]F. S. Henry, F. E. Laine-Pearson, and A. Tsuda, "Hamiltonian chaos in a model alveolus," J. Biomech. Eng. **131**, 011006 (2009).
[20]R. Sarangapani and A. S. Wexler, "Modeling aerosol bolus dispersion in human airways," J. Aerosol Sci. **30**, 1345 (1999).
[21]D. Y. Lee and J. W. Lee, "Characteristics of particle transport in an expanding or contracting alveolated tube," J. Aerosol Sci. **34**, 1193 (2003).
[22]C. Darquenne and G. K. Prisk, "Effect of gravitational sedimentation on simulated aerosol dispersion in the human acinus," J. Aerosol Sci. **34**, 405 (2003).
[23]C. Darquenne and G. Kim Prisk, "Effect of small flow reversals on aerosol mixing in the alveolar region of the human lung," J. Appl. Physiol. **97**, 2083 (2004).
[24]G. Xia and C.-L. Lin, "An unstructured finite volume approach for structural dynamics in response to fluid motions," Comput. Struct. **86**, 684 (2008).
[25]G. Xia, M. H. Tawhai, E. A. Hoffman, and C.-L. Lin, "Airway wall stiffness and peak wall shear stress: A fluid-structure interaction study in rigid and compliant airways," Ann. Biomed. Eng. **38**, 1836 (2010).
[26]H. Kumar, C.-L. Lin, M. H. Tawhai, and E. A. Hoffman, "The effects of geometry on airflow in the acinar region of the human lung," J. Biomech. **42**, 1635 (2009).
[27]G. Pedrizzetti, "Unsteady tube flow over an expansion," J. Fluid Mech. **310**, 89 (1996).
[28]H. Wang, P. Iovenitti, E. Harvey, and S. Masood, "Numerical investigation of mixing in microchannels with patterned grooves," J. Micromech. Microeng. **13**, 801 (2003).
[29]E. P. L. Roberts and M. R. Mackley, "The simulation of stretch rates for the quantitative prediction and mapping of mixing within a channel flow," Chem. Eng. Sci. **50**, 3727 (1995).
[30]I. J. Sobey, "Dispersion caused by separation during oscillatory flow through a furrowed channel," Chem. Eng. Sci. **40**, 2129 (1985).
[31]W. H. Lyne, "Unsteady viscous flow over a wavy wall," J. Fluid Mech. **50**, 33 (1971).
[32]P. W. Duck and R. J. Bodonyi, "Oscillatory flow over a semi-infinite flat plate at low Reynolds numbers," Comput. Fluids **16**, 311 (1988).
[33]N. Riley, "Steady streaming," Annu. Rev. Fluid Mech. **33**, 43 (2001).
[34]E. Larrieu, E. J. Hinch, and F. Charru, "Lagrangian drift near a wavy boundary in a viscous oscillating flow," J. Fluid Mech. **630**, 391 (2009).
[35]F. E. Fresconi and A. K. Prasad, "Secondary velocity fields in the conducting airways of the human lung," J. Biomech. Eng. **129**, 722 (2007).
[36]E. G. Flekkøy, T. Rage, U. Oxaal, and J. Feder, "Hydrodynamic irreversibility in creeping flow," Phys. Rev. Lett. **77**, 4170 (1996).
[37]Y. K. Suh and S. Kang, "Acoustic streaming," *Encyclopedia of Microfluidics and Nanofluidics* (Springer, New York, 2008), Part 1, pp. 25–33.
[38]J. M. Ottino, *The Kinematics Of Mixing: Stretching, Chaos And Transport, Cambridge Texts in Applied Mathematics* (Cambridge University, Cambridge, England, 1989).
[39]J. L. Helman and L. Hesselink, "Visualizing vector field topology in fluid flows," IEEE Comput. Graphics Appl. **11**, 36 (1991).
[40]W. H. Finlay, *The Mechanics of Inhaled Pharmaceutical Aerosols* (Academic, London, 2001).
[41]W. Hofmann and L. Koblinger, "Monte Carlo modeling of aerosol deposition in human lungs. Part II: Deposition fractions and their sensitivity to parameter variations," J. Aerosol Sci. **21**, 675 (1990).
[42]W. Hofmann, E. Pawlak, and R. Sturm, "Semi-empirical stochastic model of aerosol bolus dispersion in the human lung," Inhalation Toxicol. **20**, 1059 (2008).
[43]J. Wang, L. Feng, J. M. Ottino, and R. Lueptow, "Inertial effects on chaotic advection and mixing in a 2D cavity flow," Ind. Eng. Chem. Res. **48**, 2436 (2009).
[44]M. H. Tawhai and C.-L. Lin, "Image-based modeling of lung structure and function," J. Magn. Reson Imaging **32**, 1421 (2010).